Department of Physics
Division of Atomic Physics

February 6, 2017

Evaluation of white-light generation as possible seed for a mid-infrared optical parametric chirped pulse amplifier

Performed by:

Chuang Lu[1]

Supervisor: Cord Arnold[2]
Co-supervisor: Anne L'Huillier[3]

Abstract

White-light spectra of different crystals, based on 1030-nm intense pump pulses have been investigated in order to derive a near-infrared seed for mid-infrared generation. Among ten crystals, YAG (yttrium aluminium garnet), KGW (potassium gadolinium tungstate) and YVO_4 (yttrium orthovanadate) exhibit the most suitable properties for supercontinuum generation with high efficiency for spectral broadening as well as high tolerance to optical damage. Numerical simulations of laser induced filamentation, a dynamic balance between self-focusing and plasma defocusing resulting in supercontinuum generation, have been carried out to interpret and support our results theoretically. The simulations are in fair agreement with experimental results and they support the finding that low-bandgap materials like YVO_4, YAG and KGW seem to be better suited than high-bandgap materials, like fused silica and fluorides.

Thesis submitted for the degree of Master of Science
Project duration: 9 months
Date of the examination: January 2017

[1]fyk15clu@student.lu.se.com
[2]Cord.Arnold@fysik.lth.se
[3]Atomalh@fysik.lth.se

Acknowledgements

First of all, I am very thankful to Cord Arnold for enrolling me in this brilliant project as my diploma work and sending me to École polytechnique to study simulations of nonlinear processes. I have learnt a lot from his guidance and patient explanations. I also thank sincerely to Arnaud Couairon for his effort on teaching me the simulations which become large part of my thesis work.

I want to thank Neven Ibrakovic, Chen Guo and Anne Harth for teaching and training me in the use of the laser system, the spectral analyser as well as optical alignments. In addition I would like to thank all the staff at atomics physics for their warmth and kindness during this memorable period.

Finally, I want to express my gratitude to my family for their love, encouragement as well as the financial support for my whole master education at Lund University.

List of acronyms

MIR	Mid-infrared
IR	Infrared
HHG	High-harmonic generation
THG	Third-harmonic generation
SHG	Second-harmonic generation
OPA	Optical parametric amplification
OPAs	Optical parametric Amplifiers
OPACPA	Optical Parametric Chirped-pulse Amplification
OPACPAs	Optical Parametric Chirped-pulse Amplifiers
CaF_2	Calcium fluoride
BaF_2	Barium fluoride
MgF_2	Magnesium fluoride
KGW	Potassium gadolinium tungstate
Yb:KGW	Ytterbium-doped potassium gadolinium tungstate
YAG	Yttrium orthovanadate
KDP	Potassium dideuterium phosphate
YVO_4	Yttrium orthovanadate
CEP	Carrier-envelop phase
GVD	Group velocity dispersion
SFM	Self phase modulation
NA	Numerical aperture
MW	Megawatt
TW	Terawatt
D-scan	Dispersion-scan
2-D	Two-Dimensional
MIIPS	Multiphoton intrapulse interference phase scan

Contents

1 Introduction

Motivation for mid-infrared (MIR) generation

The rapid development of mid-infrared (MIR) pulsed sources in recent years is to be attributed to both newfound and improving traditional materials. The MIR light has provided better view of atoms, molecules and solids as well as a variety of applications, such as non-invasive surgery and the observation of atmospheric reactions. In particular, absorption spectroscopy benefits significantly from MIR sources because a large number of molecule absorptions exist in the MIR region (so-called 'molecular fingerprint'), which makes the MIR useful in the field of molecular sensing [1]. For instance, water and polymer exhibit very strong absorption lines in the MIR region, which facilitate applications in medicine and mechatronics [1]. Furthermore, intense MIR pulses can also be used in high-harmonic generation (HHG) to the soft X-ray range. As is known, the HHG is formed when the atomic potential is strongly deformed by a optical field which allows tunnel ionization of an electron wave packet through the potential barrier. The electron will be further accelerated by the field once driven away from the atom. As the sign of the field changes, the electron will slam back onto the atom where it recombines and interferes with the bond part of the electron wave thus generating extreme-ultraviolet (EUV) light, which is also the so-called HHG. The photon energy of the EUV increase with increasing carrier wavelength.As a result, unlike near infrared driving pulses, MIR pulses allow increasing the photon energy of HHG to the soft-x-ray spectral range [2]. In addition, it is much easier for MIR pulses to drive HHG in a condensed medium since the optical damage caused by multi-photon excitation is less pronounced for MIR driving [2]. At present, there are mainly four typical sources for MIR operating from continuous wave to femtosecond pulse duration. They are fiber laser, semiconductor laser, solid-state laser, and nonlinear sources. Nonlinear processes allow much higher conversion efficiency in ultra-short generation than in continuous generation. Therefore, nonlinear optical processes are one of the promising ways to generate MIR pulses.

In this project, we aim at investigating ways for generating MIR pulses, using optical parametric amplification (OPA) techniques. The pump energy from higher frequency wave ν_p is converted into signal ν_s and idler waves ν_i according to energy conservation $\nu_p = \nu_i + \nu_s$ due to nonlinear effects of a medium, as illustrated in Figure 1 (a) [3].

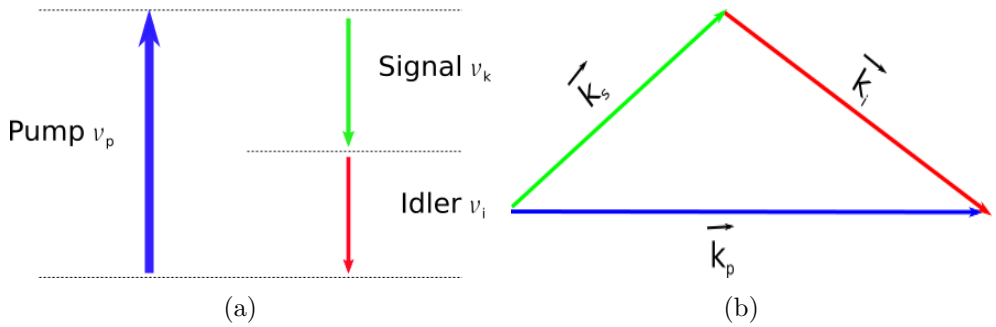

Figure 1: The energy conservation of the OPA process in three virtual states and the relevant momentum conservation.

The momentum always needs to be satisfied, $\boldsymbol{k_p} = \boldsymbol{k_i} + \boldsymbol{k_s}$, also for narrow bandwidth (see Figure 1 (b)). This usually corresponds to a collinear OPA process $k_p = k_i + k_s$ for MIR OPA (k denotes the wave vector). The momentum conservation can usually be satisfied in birefringent crystals that allow tunable refractive index dependence of the orientated (cut) angles θ to optical axis, as given by

$$\nu_s n_{\nu_s,e,\theta} + \nu_i n_{\nu_i,e,\theta} = \nu_p n_{\nu_p,o} \tag{1.1}$$

where n is the frequency and orientation dependence of the refractive index. Here, o denotes the ordinary polarization with a refractive index independent from the orientated angle θ and e denotes the extraordinary polarization with a refractive index dependent on the orientated angle.

Supercontinuum emission

Our approach is based on a Pharos laser system emitting pulses at 1030 nm. This laser is considered to pump an OPA with the signal in the range of 1.4 to 1.6 μm, resulting in an idler wave between 3 to 4 μm according to the energy conservation. In our approach, the signal could expediently be driven as well as pumped by the same laser source. The signal wave can originate from the so-called supercontinuum generation. Supercontinuum is a broadband spectrum caused by a collection of nonlinearities acting together upon a intense laser pulse, as indicated in Figure 2. Then the signal in near-infrared region can be selectively filtered out from this broad-band spectrum as the while-light seed for MIR generation. Such white-light seeded operation has a big advantage that the generated MIR idler can be possibly carrier-envelop phase stable [4].

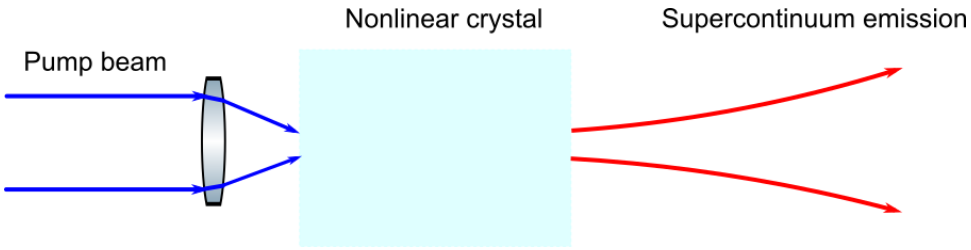

Figure 2: The blue curve indicates the input laser beam. The square box is the medium where nonlinearities takes place. The red curve indicates the supercontinuum output.

Supercontinuum emission was firstly found in the 1960s and has been developed rapidly in the last decade. It is a phenomenon in which a high power pulse can be converted to light with super-broad band spectrum due to a collection of nonlinear processes. The supercontinuum originates from the formation of the laser-induced filamentation, a process of laser pulse undergoing self-guiding [5] as well as both temporal and spatial distortions. These nonlinear processes consist of self-focusing effect, self-phase modulation, multi-photon excitation followed by plasma defocusing, intensity attenuation by multi-photon and plasma absorption. And due to these effects, the fundamental spectral bandwidth can be broadened to several octaves in the extreme smooth spectral continuum. Nowadays, supercontinuum spectra are used in many applications, such as optical communication [6], fluorescence lifetime imaging [7], gas sensing [8], etc.

In our experiment, the idea is to expose different nonlinear optical materials with femtosecond pulses to generate supercontinuum spectra covering a range from 1.4 μm to 1.6 μm, which is also suitable for the following OPAs. More than ten crystals, including Sapphire, fused silica, different fluorides (CaF, BaF, MgF) as well as less common crystals, such as yttrium aluminium garnet (YAG), potassium gadolinium tungstate (KGW), potassium dideuterium phosphate (KDP) and yttrium orthovanadate (YVO_4) have been tested.

As mentioned above, the carrier-envelop phase (CEP) stability of the MIR pulses will be important in this process for some specific application, such as the generation of identical single attosecond pulses from shot to shot. The CEP drift of femtosecond pulses originates from the group velocity dispersion (GVD) in laser resonator. As a result of the GVD, there is a certain change in the carrier-envelope offset every time a pulse hits the output coupler, which shows fluctuations in frequency domain, as illustrated in Figure 3. For a laser like Pharos the CEP of consecutive pulses is unrelated to each other. 417

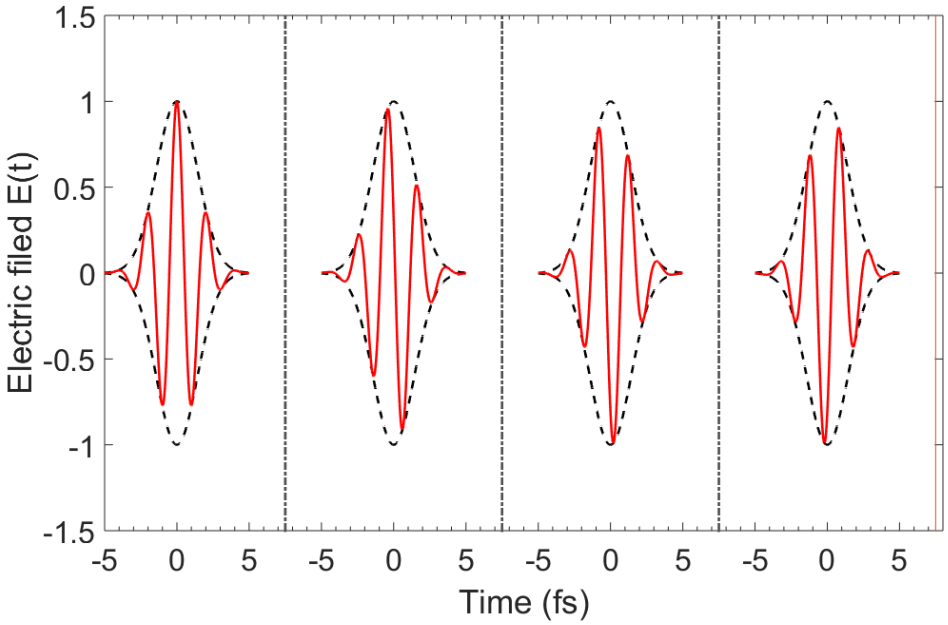

Figure 3: The CEP changes from pulse to pulse. In this graph the CEP drift $\Delta\phi = 0.4\pi$, which is equivalent to a frequency offset $f_0 = f_r \cdot \Delta\phi/2\pi$ in frequency domain, where f_r is the laser repetition rate [9].

However, the new frequencies built up from supercontinuum generation inherit the original values of the CEP [4]. This allows that the CEP drifts of both the fundamental pump and the supercontinuum seed cancel each other out in the parametric process resulting in a generation of a CEP-stable idler wave in the MIR range [4]. For OPA the bandwidth of the generated idler wave depends on the phase-matching bandwidth which is determined by the employed nonlinear material as well as by the spectral bandwidth of the signal wave from the generated supercontinuum. However, similarly important is the spectral phase of the signal wave, i.e, if the spectral phase is not compressible, the idler wave will not be compressible as well.

Numerical simulations of the supercontinuum generation were carried out to help interpreting our results. The simulation code, written by a collaborator (Arnaud Couairon) is based on a nonlinear Schrödinger type wave propagation equation, including effects such as dispersion and diffraction, self-focusing, ionization and plasma defocusing [10].

2 Theory

2.1 Laser induced filamentation

As discussed in the following, self-focusing and multi-photon ionization followed by plasma-defocusing are the primary factors resulting in supercontinuum generation. A simple propagation diagram of a laser pulse in a medium due focusing and defocusing effect is illustrated in Figure 4 [11].

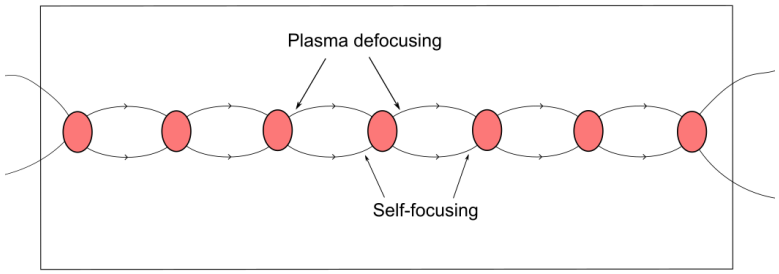

Figure 4: The refocusing (defocusing) cycles of self-focusing and plasma-defocusing form a periodic beam path.

A laser pulse carrying instantaneous powers above a certain power would undergo beam collapse. However, the beam does not collapse to a point and the intensity does not grow to infinity because plasma-defocusing will become efficient at some points in the medium. After the beam has been defocused, the pulse might still carry enough power for self-focusing, which could refocus the beam again. The periodic structure in a medium is the so-called optical filamentation. Optical filamentation is also a process of self-guiding that avoids diffraction and lead to accumulation of nonlinearity. Figure 5 illustrates a process of self-focusing simulated in a 7-mm long crystal.

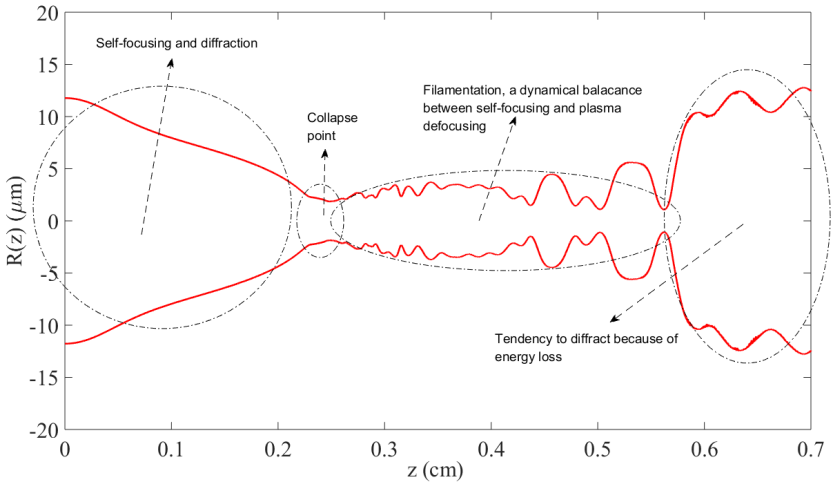

Figure 5: A simulation of self-focusing followed by filamentation.

2.2 Optical Kerr effect

Suppose the strength $\mathscr{E}(t)$ of a pulse field with center angular frequency ω_0 described by

$$\mathscr{E}(t) = \boldsymbol{Re}[E(t)\exp(i\omega_0 t)] = \frac{1}{2}E(t)\exp(i\omega_0 t) + \frac{1}{2}E^*(t)\exp(-i\omega_0 t), \tag{2.1}$$

where $E(t)$ and $E^*(t)$ are the complex envelop and complex conjugate in the temporal domain.

In a nonlinear dielectric medium, the relation between the polarization density $\mathscr{P}$ and the electric field $\mathscr{E}$ can be expressed as a power series

$$\mathscr{P} = a_1\mathscr{E} + a_2\mathscr{E}^2 + a_3\mathscr{E}^3 + ... \tag{2.2}$$

where $a_1, a_2, ..., a_n$ are constants (scalar values for isotropic medium) determined by derivatives of $\mathscr{P}$ with respect to $\mathscr{E}$ [13]. Here, $a_1 = \epsilon_0\chi$ where ϵ_0 is the dielectric constant and χ is the linear susceptibility which is related to the refractive index of the medium. The second term is the second-order nonlinearity. And the third term $a_3\mathscr{E}^3$ of the series can be expressed as

$$\mathscr{P}_{nl} = 4\chi^{(3)}\mathscr{E}^3 \tag{2.3}$$

where $\chi^{(3)}$ denotes the third order susceptibility. Those higher order polarizations (more than 3rd order) with only tiny conversion efficiencies are usually neglectful. The actual high-harmonic generations are actually formed by chain processes of wave-mixing between the second-harmonic and fundamental waves.

Substituting Equation 2.1 into 2.3, results in

$$\begin{aligned}\mathscr{P}_{nl} &= [\frac{1}{2}\chi^{(3)}E^3(t)\exp(i3\omega_0 t) + \frac{1}{2}\chi^{(3)}E^{*3}(t)\exp(-i3\omega_0 t)] + \\ &[\frac{3}{2}\chi^{(3)}E^2(t)E^*(t)\exp(i\omega_0 t) + \frac{3}{2}\chi^{(3)}E^{*2}(t)E(t)\exp(-i\omega_0 t)] \\ &= \boldsymbol{Re}[\chi^{(3)}E^3(t)\exp(i\omega_0 t)] + \boldsymbol{Re}[3\chi^{(3)}|E(t)|^2E(t)\exp(i\omega_0 t)].\end{aligned} \tag{2.4}$$

The first term inside $\boldsymbol{Re}[]$ of the right-hand side corresponds to the complex polarization:

$$P_{nl}^{(3)}(t) = \chi^{(3)}E^3(t)\exp(i3\omega_0 t) \tag{2.5}$$

of the third-harmonic generation (THG) at center frequency $3\omega_0$. Usually, the third order susceptibilities are very small values, so the conversion efficiency to THG is very low compared to the linear frequency generation at high laser intensity. In fact, as mentioned above, the actual THG generation is usually generated through second-harmonics generation followed by sum-frequency generation of the second-harmonic and the fundamental waves [12].

The second term of $\mathscr{P}_{nl}$ inside $\boldsymbol{Re}[]$, centered at the fundamental frequency ω_0, given by

$$P_{nl}(t) = 3\chi^{(3)}|E(t)|^2E(t)\exp(j\omega_0 t) \tag{2.6}$$

leads to an incremental change in susceptibility $\Delta\chi$:

$$\Delta\chi = \frac{P_{nl}(t)}{E(t)} = 3\chi^{(3)}|E(t)|^2 = 6\cdot\frac{\chi^{(3)}\eta I}{\epsilon_0} \tag{2.7}$$

where $I = |E(w)|^2/2\eta$ is the optical intensity; ϵ_0 is the vacuum permittivity. The impedance $\eta = \sqrt{\mu_0/\epsilon}$ is defined by the impedance η_0 of free space as $\eta = \eta_0/n$. A change in susceptibility is equivalent to to an incremental index of refraction $\Delta n = \frac{\Delta\chi}{2n}$. Combining the equations above yields:

$$n(I) = n + n_2 I, \tag{2.8}$$

where

$$n_2 = \frac{3\eta}{n^2\epsilon_0}\chi^{(3)} \tag{2.9}$$

is called Kerr index or nonlinear refractive index. The change in total refractive index is therefore proportional to the optical intensity I.

The Kerr indices of crystals we used are indicated in Table 1.

Crystal	MgF_2	CaF_2	KDP	BaF_2	Fused Silica	Sapphire	YAG	KGW	YVO_4
Kerr index ($10^{-16}cm^2/W$)	0.91[14]	1.24[15]	1.56[16]	2.0[17]	3.2[18]	3.06[19]	6.5[20]	10[21]	15[21]
Band gap (eV)	10.8[22]	12.1[23]	7.12[24]	9.1[25]	9.0 [27]	10[27]	7.9[27]	5.9[27]	3.9[27]

Table 1: The Kerr index and band gap of different crystals

It is given a laser pulse with a space-time intensity profile $I(r,t)$. The phase $\Delta\varphi$ introduced by the Kerr effect is given by

$$\Delta\varphi(t) = -\int \frac{\partial I(r,t)}{\partial z} k_0 \mathrm{d}z \tag{2.10}$$

where $k_0 = \omega_0/c$ is the propagation wave number and z is the traveling distance in the medium. Therefore, the introduced phase is equivalent to the change in the instantaneous frequency $\Delta\omega_i$ given by

$$\Delta\omega_i = \frac{\partial\Delta\varphi(t)}{\partial t} = -n_2\frac{\omega_0}{c}\int \frac{\partial I(r,t)}{\partial z\partial t}\mathrm{d}z. \tag{2.11}$$

The phenomenon is the so-called self phase modulation (SPM), which leads to spectral broadening of the laser pulse caused by the Kerr effect. From Equation 2.11 the red frequency components $-\Delta\omega$ are generated in the leading part of the pulse and the blue frequency components are generated in the trailing half, since the new frequency components depend on the slope of the pulse with respect to time, as illustrated in Figure 6 [28].

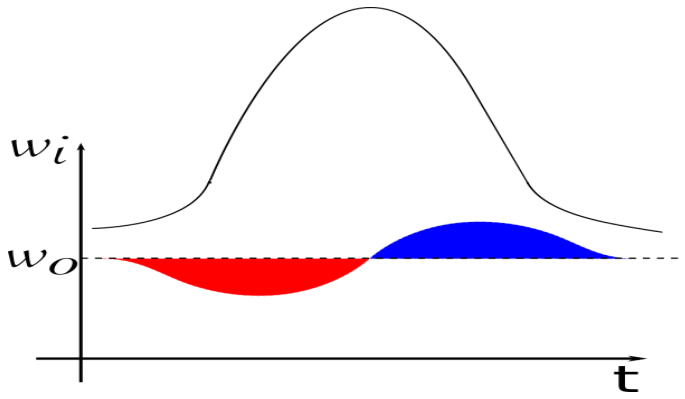

Figure 6: The temporal profile of laser pulse and its corresponding $\Delta\omega_i$ generation with time.

Because the intensity profile of the laser pulse $I(r,t)$ has intensity distribution along the transverse plane, the refractive index can be written in the form of $n(r,t) = n + n_2 I(r,t)$ of which the maximal value is usually in the center of the beam and decrease away from the center. As a result, the phase introduced by the spatial variance of the refractive index decreases with distance to the center. This is the so-called self-focusing effect, acting like a convex lens that bends wave fronts leading to focusing.

There is a critical power P_{cr} above which the focusing effect overcomes diffraction and leads to the collapse of the beam. P_{cr} is given by

$$P_{cr} = \frac{a\lambda_0^2}{8\pi n_0 n_2}, \tag{2.12}$$

where a is a constant specified by the beam profile. For a Gaussian beam, $a = 3.72$. λ_0 is the center wavelength of the laser [29].

The collapse distance L_c at which a beam, entering a nonlinear medium at the position of the waist, focuses to a singularity in absence of dispersion and plasma is given numerically by

$$L_c = \frac{0.367 z_0}{\sqrt{[(P_{in}/P_{cr})^{0.5} - 0.852]^2 - 0.0219}}, \tag{2.13}$$

where z_0 is the Rayleigh length of the initial Gaussian beam in linear propagation [29] [30]. If a lens is used to transform the input beam profile, the collapse distance L_{cf} Equation 2.13 is modified to [29] [30]

$$\frac{1}{L_{cf}} = \frac{1}{L_c} + \frac{1}{f}, \tag{2.14}$$

where f denotes the focal length of the lens.

In the experiment, the initial beam waist on mili-meter scale. Equation 2.13 would predict an impractically long collapse length of lens of centimeters. Therefore, lenses are always used in order to facilitate supercontinuum generation, which avoids the uses of long materials. L_{cf} here also marks the distance in the medium at which the most nonlinear processes, such as plasma effects, happen.

2.3 Multi-photon ionization

Multi-photon ionization (MPI) is a phenomenon that the energy of several identical photons add together in order to ionize atoms or molecules with band gap much larger than the photon energy. Because the free electrons are generated, MPI also leads to plasma generation. Since multi-photon ionization of a medium always requires the simultaneous absorption of a substantial number of photons, this process is highly dependent on the laser radiation intensity I. In this case, only at high energy laser pulses make it possible. The ionization rate described by perturbation theory [31], is proportional to I^N where N is an integer depending on the photon energy and the medium, for instance, $N = 8$ for oxygen at 800 nm [32].

The generated plasma due to MPI causes a decrease in the local refractive index, given by

$$n \approx n_0 - \frac{\rho(r,t)}{2\rho_c} \tag{2.15}$$

where ρ is the free electron density and ρ_c denotes the critical plasma density above which the plasma turns opaque [33]. ρ_c at excitation frequency ω_0 is given by

$$\rho_c = \frac{\epsilon_0 m_e \omega_0^2}{e^2} \tag{2.16}$$

where m_e is the electron mass and e is the electron charge. ρ_c is usually on a scale of 10^{21} cm^{-3} and the typical density (the maximal plasma density in our simulations) in a solid is usually on a scale of 10^{19} cm^{-3} [33]. The refractive index in Equation 2.16 is an inverse effect of self-focusing according to Equation 2.8. Likewise a reduction in the refractive index acts as concave lens that defocuses the laser beam, the plasma density ρ build up the fastest at the peak of the pulse. So the leading part of the pulse usually only experiences low electron density and thus no plasma defocusing, whereas the trailing edge can experience strong plasma defocusing. The sudden drop in refractive index contributes to a spectral broadening towards the blue frequency regime. The differential instantaneous frequency $\Delta\omega_p$ by the plasma effect is given by (for convenience, the intensity modulation along propagation distance is not considered, which implies that $I(r,t)$ is independent from the propagation distance z)

$$\Delta\omega_p = \frac{\omega_0 z}{2n_0\rho_c c}\frac{\partial\rho(r,t)}{\partial t} \tag{2.17}$$

By combining Equation 2.17 and 2.11, the overall frequency $\omega(t)$ can be written as

$$\omega(t) = \omega_0 + \frac{\omega_0 z}{c}(-n_2\frac{\partial I(r,t)}{\partial t} + \frac{1}{2n_0\rho_c}\frac{\partial\rho(r,t)}{\partial t}) \tag{2.18}$$

The plasma-defocusing length L_{pl} is given by [32]

$$L_{pl} = \frac{2n_0\rho_c}{k_0\rho_a}. \tag{2.19}$$

where ρ_a denotes the atom density corresponding to complete ionization. L_{pl} is defined as a specific distance over which the integrated nonlinear phase varies by a factor of one from complete ionized plasma when $\rho = \rho_a$.

2.4 Plasma absorption and multi-photon absorption

Subsequently, the electrons generated in the multi-photon ionization process will acquire kinetic energy by being accelerated by the electric field of the remaining part of the laser pulse. The kinetic energy will allow the further impact ionization of other molecules to generate more electrons. The phenomenon is the so-called electric breakdown which will prevent the laser pulses to propagate through long distance due to the energy loss.

In the Drude model, the electronic plasma can be treated as a fluid where the instantaneous collision between free electrons that move against heavy molecules (atoms) is the only possible interaction taking place to alter their velocities while any other long-range interactions such as the electromagnetic force neither with other electrons nor with ions are considered. The current density $\mathscr{J}$ of free electrons induced by the electric field is governed by

$$\frac{d\mathscr{J}}{dt} = \frac{e^2}{m_e}\rho\mathscr{E} - \frac{\mathscr{J}}{\tau_c} \tag{2.20}$$

and $\mathscr{J} = \rho e\mathbf{v}$ where $\mathbf{v}$, ρ, and m_e denote the collective electron velocity, the plasma density and the electron mass. τ_c that is independent of both electron position or velocity denotes the phenomenological mean time between collisions [34]. The solution of Equation 2.20 in the frequency domain reads

$$\mathscr{J} = \frac{\tau_c(1+i\omega\tau_c)\rho e^2\mathscr{E}}{(1+\omega^2\tau_c^2)m_e}, \tag{2.21}$$

where ω is the frequency of the electric field [34]. So that the absorption of the plasma is governed by [35]

$$\frac{1}{2}\mathscr{J}\cdot\mathscr{E}^* = \frac{\tau_c e^2\rho|\mathscr{E}|^2}{2(1+\omega^2\tau^2)m_e}. \tag{2.22}$$

Unlike the plasma absorption in the Drude model, multi-photon absorption also attenuates the beam energy. The energy loss due to multi-photon absorption can be described by the so-called dissipative current $\boldsymbol{J}_k$. governed by

$$\boldsymbol{J}_k\cdot\mathscr{E} = \rho_k\sigma_k I^k U_i \tag{2.23}$$

where ρ_k, σ_k, I^k, and $U_{i,k}$ are atom density, ionization cross section, field intensity and ionization potential. Here

$$k = \frac{U_i}{\hbar\omega_0} + 1 \tag{2.24}$$

specifies the species (or bandgap U_i) as well as the number of photons necessary to ionize an free electron ($\hbar$ is the Plank constant).

2.5 Self-steepening

Self-steepening is another impact of the Kerr effect. In the temporal domain the central part of the pulse experiences higher refractive index indicated by Equation 2.8 than that of the edges of the pulse, so that the light velocity in a medium slows down as the intensity increases. As a consequence, the trailing edge of the pulse will run into the

peak, leading to a steep trailing edge, referred to as self-steepening or shock formation. As a result in the frequency domain, self-steepening generates more broadening towards blue frequencies.

2.6 Raman delay

For a longer pulse duration (longer than 100 fs), the laser induced Kerr effect can be modulated by a slower response, originating from the nuclear motion apart from the instantaneous response from electronic contribution [36]. This is the so-called Kerr Raman response. In a solid, the Raman-Kerr effect is described by a three-level non-resonant process between a higher virtual energy state and two lower vibrational states, which results in a noninstantaneous optical polarization [37].

The Raman response function is used to characterize the relation between the nonlinear polarization density and the electric field, as represented by Equation

$$\mathscr{P}_{nl} = \epsilon_0 Q_R(t)\mathscr{E}, \tag{2.25}$$

where $Q_R(t)$ consists of an instantaneous and a delayed contribution. The delayed response is important for pulses longer than 100 fs. Equation 2.25 will lead to [37]

$$\mathscr{P}_{nl} = 2\epsilon_0 n_0 n_2[(1-\alpha)I(t) + \alpha\int_0^\infty I(t-\tau)\mathcal{R}(\tau)\mathrm{d}\tau]\mathscr{E}(t). \tag{2.26}$$

Here, the instantaneous and delayed Kerr response are presented by the first and second term on the right-hand side of Equation 2.26. α here is the fraction of the Raman delay and $\mathcal{R}(\tau)$ is a response function corresponding to the fundamental rotational frequency, phenomenological damping rate as well as the peak field amplitude. As results, the Raman response can delay Kerr effect in time as well as lengthen the collapse distance of self-focusing in space.

3 Experimental setup

3.1 Supercontinuum generation

The laser source in the experiment is a 5-μJ regenerative amplifier seeded with a high-repetition rate, 1030-nm Yb-KGW oscillator (Pharos) with the pulse duration ranging from 150 fs to 250 fs, which is close to the transform limit (the shortest pulse with a certain spectral bandwidth). In addition, the repetition rate can be decreased by a built-in pulse picker down to 1 Hz. The overall setup is illustrated in Figure 7. The pulse duration can be stretched by tuning the position of the built-in compressor.

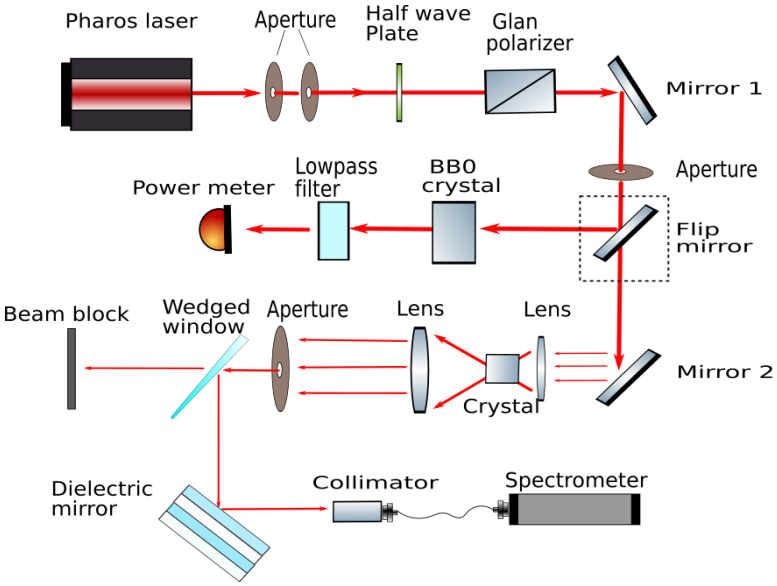

Figure 7: The primary experimental setup for supercontinuum generation

The external attenuator is made by a half-wave retarder (WPH05M-1053) and a linear polarizer (Glan-Taylor Polarizer, GT10-B) in sequence, as illustrated in Figure 8.

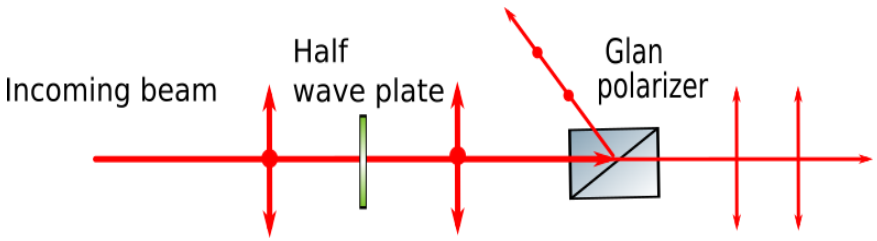

Figure 8: A sketch of the external attenuator

The principle of the attenuator is based on Malus' law. Suppose an angle θ between the beam polarization and the primary axis of the polarizer. The wave retarder is fixed in a rotational mount that allows continuous rotation of the beam's polarization direction. The variable output power P according to Malus's law is given by

$$P = P_0 \cos^2(\theta), \tag{3.1}$$

where P_0 denotes the initial laser power. We use a flip mirror to send optionally the beam to a BBO crystal. We can then move the compressor of the laser to maximize the second harmonic yield and by that obtain transform-limited pulses.

Different lenses are used to focus the beam into different crystals for supercontinuum generation. Also other lenses after the crystals are used to select the bright core of the filament. A wide-range spectral analyser connected to a collimator (f=15.52 mm, NA=0.15, F260FC-C) with a optical fiber (D=50 μm, NA=0.22, M42L01) is used to record the supercontinuum spectra. Different dielectric mirrors and spectral filters are used to select the desired spectral range to be measured. In addition, wedged windows or prisms allow to select a tiny amount of the laser power before the spectral measurement.

4 Numerical model

We start from the wave propagation in a nonlinear medium governed by Maxwell's equations. The relations among electric field $\boldsymbol{E}$, magnetic field $\boldsymbol{H}$, electric flux density $\boldsymbol{D}$, electric current density $\boldsymbol{J}$ and magnetic flux density $\boldsymbol{B}$ are:

$$\nabla \cdot \boldsymbol{D} = 0, \tag{4.1}$$

$$\nabla \cdot \boldsymbol{B} = 0, \tag{4.2}$$

$$\nabla \times \boldsymbol{E} = -\frac{\partial \boldsymbol{B}}{\partial t}, \tag{4.3}$$

$$\nabla \times \boldsymbol{H} = \frac{\partial \boldsymbol{D}}{\partial t} + \boldsymbol{J}, \tag{4.4}$$

where $\nabla\cdot$ and $\nabla\times$ denote the divergence and curl operators. It should be noted that the right-hand side of the Gaussian law in Equation 4.1 vanishes in stead of equalling to the electron density ρ in cases where the electron densities are much smaller than atomic densities (The electron density is up to 10^{19} cm^{-3} in our simulations and the atomic density for a solid is usually on a scale of 10^{25} cm^{-3}) [38]. $\boldsymbol{D}$ and $\boldsymbol{E}$ are linked by

$$\boldsymbol{D} = \epsilon_0 \boldsymbol{E} + \boldsymbol{P}_l + \boldsymbol{P}_{nl}. \tag{4.5}$$

The electric $\boldsymbol{E}$ can be considered as a superposition of waves with different central frequencies. In coupled-wave theory, the wave equation can be separated into many harmonic functions of specific frequencies. So each frequency component can be treated individually and the outcome can be also written as superposition of all these harmonic oscillations [39]. For our simulation, we only consider the linear frequency component contributed from the first and the third order polarization density. In fact, the high-order frequency generation which requires very strict conditions usually have very low conversion efficiency during the supercontinuum generation (SHG has been experimentally observed).

The polarization vector $\boldsymbol{P} = \boldsymbol{P}_l + \boldsymbol{P}_{nl}$ containing linear and nonlinear terms of the electric field is given by Equation 2.2. In a nonmagnetic medium, $\boldsymbol{B} = \mu_0 \boldsymbol{H}$, where μ_0 denotes the permeability of free space.

Then, the curl $\nabla\times$ of Equation 4.3 is taken, which results in:

$$\nabla \times \nabla \times \boldsymbol{E} = \nabla(\nabla \cdot \boldsymbol{E}) - \nabla^2 \boldsymbol{E}. \tag{4.6}$$

In nonlinear media, the first term on the right-hand side does not vanish even for isotropic media. According to Equation 4.5 in nonlinear optics $\nabla \cdot \boldsymbol{D} = 0$ does not imply $\nabla \cdot \boldsymbol{E} = 0$. However this term is usually dropped for most cases in nonlinear optics especially for infinite plane wave as well as the slowly varying amplitude approximation [40]. Then we substitute Equation 4.4 and 4.5 in 4.6 while we neglect the first term on the right-hand side of Equation 4.6, what results in

$$\nabla^2 \boldsymbol{E} - \frac{1}{\epsilon c^2} \frac{\partial^2 (\epsilon_0 \boldsymbol{E} + \boldsymbol{P}_l)}{\partial t^2} = \frac{1}{\epsilon_0} \frac{\partial^2 \boldsymbol{P}_{nl}}{\partial t^2} + \frac{\partial \boldsymbol{J}}{\partial t}. \tag{4.7}$$

Here the linear part of the displacement field $\boldsymbol{D}_l$ is given by:

$$\boldsymbol{D}_l = \epsilon_0 \boldsymbol{E} + \boldsymbol{P}_l = \epsilon_0 \boldsymbol{\epsilon} \boldsymbol{E}, \tag{4.8}$$

where $\boldsymbol{\epsilon}$ denotes the frequency-dependent dielectric tensor. For an isotropic medium, the equation reduces to

$$\boldsymbol{D}_l = \epsilon_0 \epsilon \boldsymbol{E} = \epsilon_0 n^2 \boldsymbol{E}. \tag{4.9}$$

ϵ becomes a scalar and n is the frequency-dependent refractive index of the medium. For a non-dispersive pure Kerr medium, as shown in Equation 2.6, $\boldsymbol{P}_{nl}$ is given by

$$\boldsymbol{P}_{nl} = 3\chi^{(3)} |\boldsymbol{E}|^2 \boldsymbol{E}. \tag{4.10}$$

4.1 Nonlinear Schrödinger equation

We start with a medium without plasma generation where the induced current density term $\boldsymbol{J}$ in Equation 4.7 is 0. Combining Equation 4.7 and 4.9 gives

$$\nabla^2 \boldsymbol{E} - \frac{(n^2 + 2n_0 n_2 I)}{c^2} \frac{\partial^2 \boldsymbol{E}}{\partial t^2} = 0 \tag{4.11}$$

where $I = c\epsilon_0 n |\boldsymbol{E}|^2/2$ denotes the field intensity and the wave number is $k_0 = \omega/c$ in free space.

Because the divergence of laser-induced filamentation are relatively small, the spatial envelop of the electric field as well as its derivative with its propagation distance vary slowly within the length of a wavelength. So the slowly-varying electric field $\boldsymbol{E}$ from this small-angle approximation can be introduced in Equation 4.11 represented by

$$\boldsymbol{E}(\boldsymbol{r}, t) = \boldsymbol{A}(\boldsymbol{r}) \cdot T(t) \exp[i(kz - \omega_0 t)], \tag{4.12}$$

where $\boldsymbol{A}(\boldsymbol{r})$ and $T(t)$ are the complex envelop in space and time domains respectively. We substitute Equation 4.12 in 4.11 and use the technique of separation of variables that leads to

$$\begin{aligned} \frac{\nabla^2 \{\boldsymbol{A}(\boldsymbol{r}) \exp(ikz)\}}{\boldsymbol{A}(\boldsymbol{r}) \exp(ikz)} = \frac{(n^2 + 2n_0 n_2 I)}{c^2} \frac{\partial^2}{\partial t^2} (T(t) \exp(-i\omega_0 t)) \\ = -k_0^2 (n^2 + 2n_o n_2 I). \end{aligned} \tag{4.13}$$

The left-hand side of Equation 4.13 reads

$$\nabla^2 \boldsymbol{A}(\boldsymbol{r}) + i2nk_0 \frac{\partial \boldsymbol{A}(\boldsymbol{r})}{\partial z} + k_0^2 c\epsilon_0 n_2 n^2 |\boldsymbol{E}|^2 \boldsymbol{A}(\boldsymbol{r}) = 0. \tag{4.14}$$

Since the envelop $\boldsymbol{A}(\boldsymbol{r})$ itself varies slowly with propagation distance within the length of a wavelength. Compared to other terms such as $\partial \boldsymbol{A}(\boldsymbol{r})/\partial z$ and $\partial^2 \boldsymbol{A}(\boldsymbol{r})/\partial x^2$, the higher order derivative $\partial^2 \boldsymbol{A}(\boldsymbol{r})/\partial z^2$ in the Laplacian operation due to the small-angle approximation can be neglected. Then Equation 4.14 becomes

$$\nabla_T^2 \boldsymbol{A}(\boldsymbol{r}) + k^2 c\epsilon_0 n_2 |\boldsymbol{E}|^2 \boldsymbol{A}(\boldsymbol{r}) + i2k \frac{\partial \boldsymbol{A}(\boldsymbol{r})}{\partial z} = 0 \tag{4.15}$$

where $\nabla_T^2 = (\partial^2/\partial x^2 + \partial^2/\partial y^2)$ is the transverse Laplacian operator, and $k = n_0 k_0$ is the wave number. Equation 4.15 is obtained with a reduced model by assuming a monochromatic wave where $n = n_0$ is a constant in Equation 4.11.

This time independent Equation 4.15 governing the propagation equation in pure Kerr media is the so-called nonlinear Schrödinger Equation, from which the collapse length in Equation 2.13 is derived.

4.2 Model including dispersion, absorption, Raman contribution, recombination and avalanche ionization

For dispersive, absorptive, conductive media (when the plasma current play a role), the frequency dependent linear refractive index $n(\omega)$, the plasma current density in the Drude model (Equation 2.20) as well as the dissipative current in Equation 2.23 due multi-photon absorption are also considered.

Now, suppose the modulated wave equation referred to Equation 4.11 governed by

$$\nabla^2 \boldsymbol{E} - \frac{(n^2(\omega) + 2n_0 n_2 I)}{c^2} \frac{\partial^2 \boldsymbol{E}}{\partial t^2} = \mathscr{N} \boldsymbol{E}, \tag{4.16}$$

where $\mathscr{N}$ is an operator regarding the current density $\boldsymbol{J}$ in the second term of the right-hand side in Equation 4.7. Suppose a Fourier transform at center frequency ω_0, $\tilde{\boldsymbol{E}}(\boldsymbol{r}, \omega)$ given by

$$\tilde{\boldsymbol{E}}(\boldsymbol{r}, \omega) = \int \boldsymbol{E}(\boldsymbol{r}, t) \exp[i(\omega)t] \mathrm{d}t. \tag{4.17}$$

Then we substitute Equation 4.17 in 4.16, resulting in a Helmholtz equation:

$$\nabla^2 \tilde{\boldsymbol{E}} + k^2(\omega) \tilde{\boldsymbol{E}} + \omega^2 b \cdot \tilde{\boldsymbol{E}} = \mathscr{N} \tilde{\boldsymbol{E}}, \tag{4.18}$$

where $k(\omega) = \omega^2 n^2(\omega)/c^2$ is the frequency dependent wave number and $b = 2n_0 n_2 I \omega^2/c^2$ is a constant. Now, we use separation of variables again, which reads

$$\tilde{\boldsymbol{E}}(\boldsymbol{r}, \omega) = \tilde{\boldsymbol{A}}(\boldsymbol{r}, \omega) \exp(ik_0 z). \tag{4.19}$$

$\tilde{\boldsymbol{A}}$ is also a slowly varying function of z. Substituting Equation 4.19 in 4.18 leads to

$$\nabla^2 \tilde{\boldsymbol{A}} + 2ik_0 \frac{\partial \tilde{\boldsymbol{A}}}{\partial z} + [k^2(\omega) - k_0^2] + \omega_0^2 b \cdot \tilde{\boldsymbol{A}} = \mathscr{N} \tilde{\boldsymbol{A}}. \tag{4.20}$$

Here it is useful to expand $k(\omega)$ in a Taylor series around center frequency ω_0:

$$k(\omega) = k_0 + (\omega - \omega_0)k^{(1)} + \frac{1}{2}(\omega - \omega_0)^2 k^{(2)} + \cdots + \frac{1}{n!}(\omega - \omega_0)^n k^{(n)} \tag{4.21}$$

where $k^{(n)} = (\mathrm{d}^n/\mathrm{d}\omega^n)k(\omega)_{\omega=\omega 0}$. Then we make an approximation:

$$k^2(\omega) - k_0^2 \approx 2k_0(k(\omega) - k_0) \approx 2k_0[(\omega - \omega_0)k^{(1)} + \frac{1}{2}(\omega - \omega_0)^2 k^{(2)}], \tag{4.22}$$

and substitute the result back in Equation 4.23 which leads to

$$\nabla^2 \tilde{\boldsymbol{A}} + 2ik_0 \frac{\partial \tilde{\boldsymbol{A}}}{\partial z} + 2k_0[(\omega - \omega_0)k^{(1)} + \frac{1}{2}(\omega - \omega_0)^2 k^{(2)}]\tilde{\boldsymbol{A}} + \omega_0^2 b \cdot \tilde{\boldsymbol{A}} = \mathscr{N}\tilde{\boldsymbol{A}}. \tag{4.23}$$

After these simplifications, the inverse Fourier transform of $\tilde{\boldsymbol{A}}$ is taken again:

$$\boldsymbol{A}(\boldsymbol{r}, t) = \frac{1}{2\pi}\int \tilde{\boldsymbol{A}}(\boldsymbol{r}, \omega)\exp[-(i\omega t)]\mathrm{d}\omega, \tag{4.24}$$

and during the transformation, $(\omega - \omega_0)$ is replaced by the differential operator $i\partial/\partial t$. After applying the slowly varying envelop approximation, Equation 4.23 becomes

$$\frac{\partial \boldsymbol{A}}{\partial z} = \frac{i}{2k_0}\nabla_T^2 \boldsymbol{A} - ik^{(1)}\frac{\partial}{\partial t}\boldsymbol{A} - i\frac{k^{(2)}}{2}\frac{\partial^2}{\partial t^2}\boldsymbol{A} + \mathscr{N}_{\mathrm{sum}}\boldsymbol{A}, \tag{4.25}$$

where the operator $\mathscr{N}_{\mathrm{sum}}$ is a sum of the plasma absorption, Kerr effect, multi-photon absorption, Raman contribution, avalanche ionization and electron recombination. $\mathscr{N}_{\mathrm{sum}}$ is given by a operator set [37]:

$$\mathscr{N}_{\mathrm{sum}} = \mathscr{N}_{\mathrm{Kerr}} + \mathscr{N}_{\mathrm{MPA}} + \mathscr{N}_{\mathrm{Plasma}}. \tag{4.26}$$

The Kerr term $\mathscr{N}_{\mathrm{Kerr}}$ modified by Raman delayed nonlinear response is given by

$$\mathscr{N}_{\mathrm{Kerr}} = ik_0 n_2(1 - \alpha)|\boldsymbol{A}|^2 + ik_0 n_2 \alpha \int_{-\infty}^{t} \mathcal{R}(t - \tau)|\boldsymbol{A}|^2 \mathrm{d}\tau. \tag{4.27}$$

In the Drude model, as mentioned in Equation 2.21, $\mathscr{N}_{\mathrm{Plasma}}$ is related to the laser induced plasma current density:

$$\mathscr{N}_{\mathrm{Plasma}} = -\frac{\sigma(1 + i\omega_0\tau_c\rho)}{2} \tag{4.28}$$

where the cross section $\sigma = k_0\omega_0\tau_c/n_0\rho_0(1 + \omega_0^2\tau_c^2)$.

The multi-photon absorption term corresponding to the dissipative current in Equation 2.23 is given by

$$\mathscr{N}_{\mathrm{MPA}} = -\frac{\beta_k}{2}|\boldsymbol{E}|^{2k-2}(1 - \frac{\rho}{\rho_{at}}) \tag{4.29}$$

where ρ_{at} denotes the atomic density. β_k is the multi-photon ionization coefficient given by

$$\beta_k = j\hbar\omega_0\rho_{at}\sigma_k \tag{4.30}$$

where σ_k denotes the ionization cross section.

The plasma density entering in Equation 4.28 and 4.29 is governed by the multi-photon ionization rate $\sigma_k|\boldsymbol{E}|^{2k}$, avalanche ionization rate $\sigma/U_i|\boldsymbol{E}|^2$, all of which can be written as

$$\frac{\partial\rho}{\partial t} = \sigma_k|\boldsymbol{E}|^{2k}(\rho_{at}-\rho) + \frac{\sigma}{U_i}\rho\boldsymbol{E}|^2 - a\rho^2[36]. \tag{4.31}$$

where the last term $\alpha\rho$ denotes the electron-ion recombination rate. A great advantage of the propagation formula in a term of Equation 4.25 is that imaginary coefficients in charge of the phase modulation and real coefficients in charge of the intensity modulation in the right-hand side are intuitive.

4.3 Initial pulse

The boundary and initial conditions must be specified to start the simulation. Gaussian beams are assumed in the simulations. Referring to Equation 4.12, the spatial envelop $\boldsymbol{A}(\boldsymbol{r})$ entering at the beam waist is governed by

$$\boldsymbol{A}(\boldsymbol{r}) = \sqrt{\frac{2P_{in}}{\pi w_0^2}}\exp\frac{-x^2-y^2}{w_0^2}, \tag{4.32}$$

where w_0 and P_{in} are the waist radius and input power respectively. The temporal envelop $T(t)$ is governed by

$$T(t) = \exp[-\frac{(1-i\mathrm{C})t^2}{t_p^2}] \tag{4.33}$$

where t_p denotes the pulse duration and C denotes the chirp of the pulse.

5 Experimental results

5.1 Critical power for self-focusing

As discussed above, the critical power of a laser pulse at which self-focusing overcomes diffraction is an essential factor to start laser-induced filamentation and generate supercontinuum. But in our experiment, input powers needed to observe supercontinuum are always higher than the theoretical critical powers. This can be due to reflection from the crystal surface as well as the size of crystals that does not allow enough length for the self-focusing. It should also be noted that effects that can arrest self-focusing, such as dispersion and ionization, usually lead to a higher power requirement to observe filamentation and supercontinuum [41] . In the experimental setup, the laser pulse is focused with convex lenses in order to reduce the collapse length of self-focusing to the limited size of our crystals. Suppose the Rayleigh length of a Gaussian beam before focusing is much longer than the focal length f of the lens. The beam size W_0' at the focus after transformation of the lens is given by

$$W_0' = \frac{\lambda}{\pi W_0} f \tag{5.1}$$

where W_0 denotes the input beam size [42]. As a result, W_0' is on a scale of micro meters and the related Rayleigh length is on sub-milimeter scale. According to Equation 2.13, the collapse length of self-focusing is on milimeter scale ($1<P_{in}/P_{cr}<5$) which is usually shorter than the length of different crystals used for supercontinuum generation. In our experiment, the input laser power is slowly increased from 0 by tuning the external attenuator and the critical power is determined once the colorful conical emission of the supercontinuum is observed on a piece of white paper at a distance behind the material. Likewise, the power for multi-filamentation is also determined once the typical signature of multiple interfering filaments is observed. The power is measured right after the lens with a power meter. Losses due to Fresnel reflection at the surface to the crystal are subtracted. The experimentally obtained critical powers, defined by the power for which supercontinuum generation is observed for different crystals are presented in Figure 9, of which more details are indicated in Table 2.

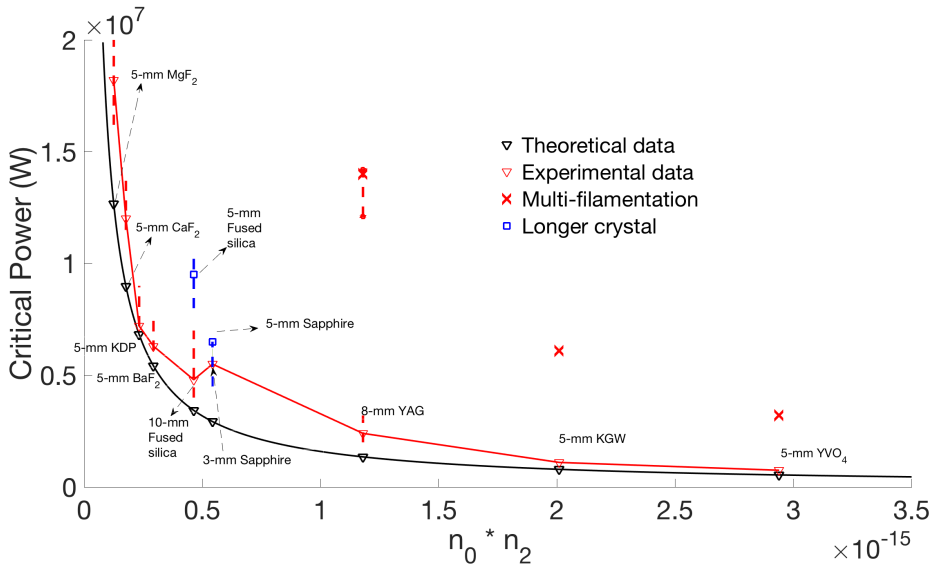

Figure 9: Critical power for different materials. The horizontal axis is the product of n_0 and n_2. The black curve indicates the theoretical critical powers calculated with Equation 2.12. The triangles mark the positions of crystals used in experiments (both red and black ones). The red curve marks the experimental results plotted the same way as explained above by using 40-mm focal length lens. The crosses mark the powers above which the single filamentation breaks to multi-filamentation. The blue squares mark the critical power of longer crystals by using 40-mm focal length lens. The dotted lines mark the variation due to the uses of different focal lengths.

Crystal	YVO_4 (5 mm)	KGW (5 mm)	YAG (8 mm)	Sapphire	Fused Silica	BaF_2 (5 mm)	KDP (5 mm)	CaF_2 (5 mm)	MgF_2 (5 mm)
$n_0 \cdot n_2$	29.4	20.0	11.8	5.43	4.64	2.93	2.33	1.77	1.26
P_{cr} (MW)	0.54	0.79	1.35	2.93	3.43	5.41	6.82	8.98	12.7
P_{ex} (MW)	0.75	1.1	2.0-3.2	4.5-6.5 (3 mm) 4.5-6.5 (5 mm)	8.0-10.05 (5 mm) 4.0-7.0 (10 mm)	6.1-7.8	7.2-8.9	11.5-14	16.2-20
Error	0.39	0.39	0.48-1.37	0.54-1.22 (3 mm) (5 mm)	1.33-1.93 (5 mm) 0.17-1.04 (10 mm)	0.13-0.44	0.05-0.3	0.28-0.56	0.28-0.57

Table 2: As obained in Figure 9, P_{ex} denotes the experimental results of the critical power for different materials and their variations due to the uses of different crystal lengths as well as focal lengths. The unit of $n_0 \cdot n_2$ is 10^{-15} cm^2 /W. Information of n_0 and n_2 are from Refractiveindex.info and Table 1.

From Figure 9, It can be seen that the practical critical powers are always bigger than the theoretical results. However, due to effects such as dispersion and plasma generation not included in the nonlinear Schrödinger equation from which Equation 2.13 was derived, the experimental power to observed filamentation is expected to be higher. The discrep-

ancy between the experimental and theoretical results seems to vanish with increasing nonlinear index because the experimental observations of supercontinuum emission are attributed to both the high enough input power and the short enough collapse distance. A crystal with a higher nonlinear index allows a shorter self-focusing collapse distance and a longer induced filament. So with increasing input laser power, this crystal will tend to emit supercontinuum earlier. Conversely, a short crystal with a long collapse distance (low nonlinear index) may not emit supercontinuum even at very high input power.

5.2 Spectral broadening

Figure 10 illustrates the results from 5-mm Sapphire by the use of a 40-mm focal length lens.

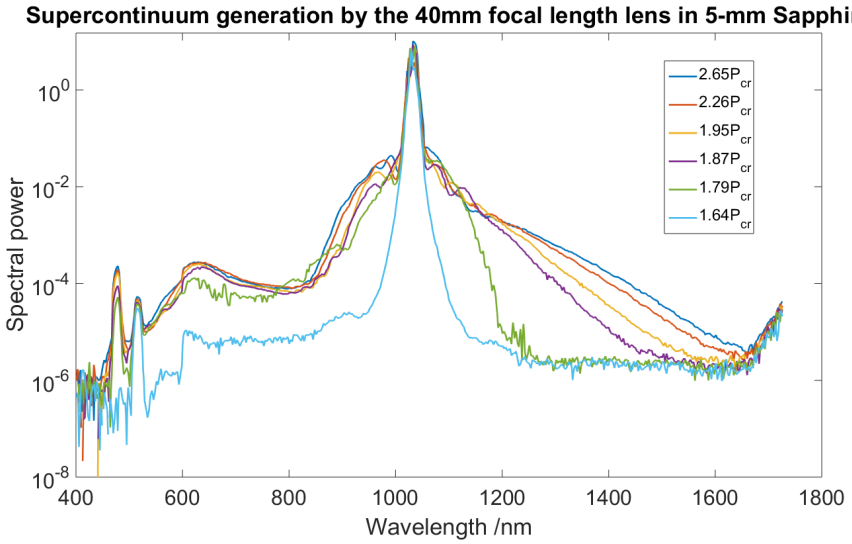

Figure 10: The spectrum of supercontinuum from Sapphire

The two secondary peaks at 485 nm and 515 nm originate from fluorescent lights in the room and SHG respectively. From the graph, we can see that the broadening increases with the input power. Larger input power leads to stronger nonlinear processes, resulting in wider spectral broadening. Figure 11 illustrates the results from 8-mm YAG crystal with the same condition.

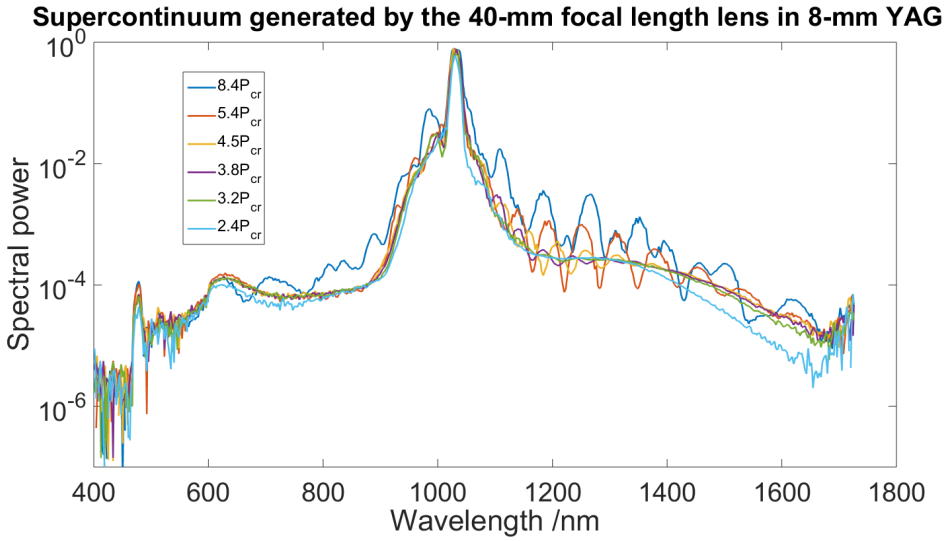

Figure 11: The spectrum of supercontinuum from YAG

Of interest here is the fluctuations in the spectral domain, when the input power is above a certain power. At very high pulse energy, the pulse split in time due to a combination of different nonlinearities, resulting in strong spectral modulation. In addition, similar spectra from 5-mm YVO_4 and 5-mm KGW are shown in Figure 12 (a) and Figure 12 (b), respectively.

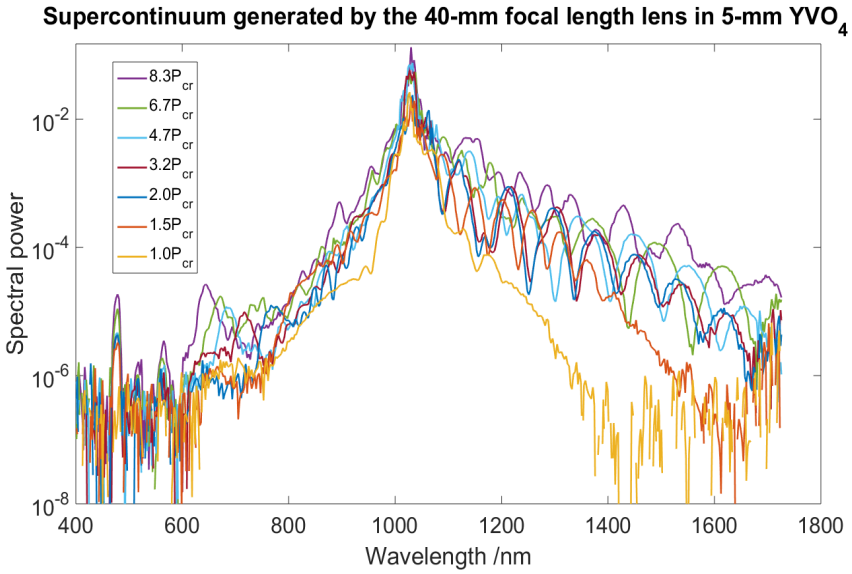

(a) The spectra from YVO_4

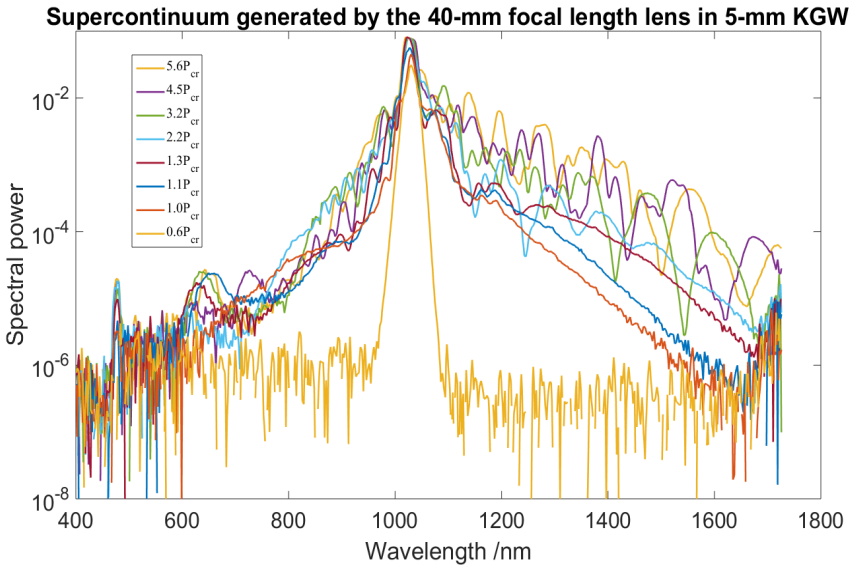

(b) The spectra from KGW

Figure 12: Supercontinuum spectra for YVO_4 and KGW

5.3 Repetition rate dependence of supercontinuum

Figure 13 illustrates the repetition rate dependence of the supercontinuum.

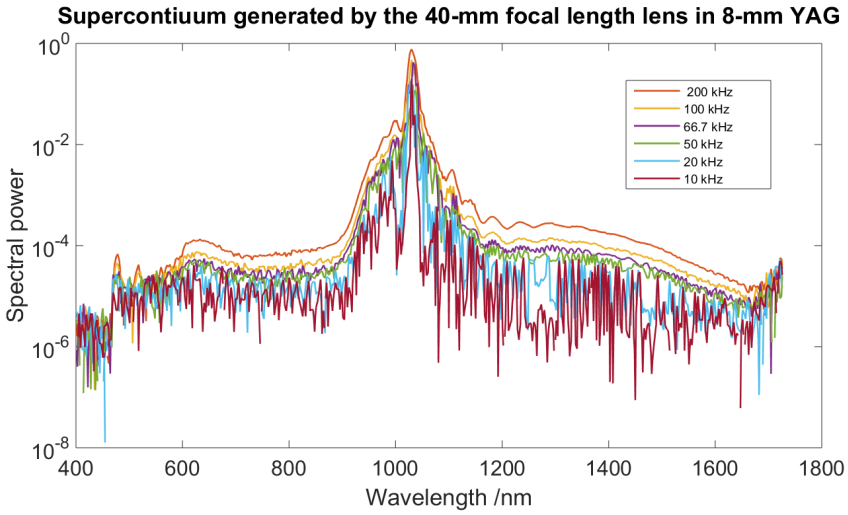

Figure 13: Spectra recorded at different laser repetition rate.

In fact, the repetition does not affect the super continuum generation because the formation of filamentation is determined by the single pulse individually (the simulations are also done with a single pulse). From the graph, at very low repetition rate down to 10 kHz, the fast fluctuation in the spectra is due to the insensitivity of the untriggered spectrometer at low repetition rate. But the repetition rate is very important: it directly links to the accumulative damage of the material with low optical damage tolerance (in our experiment, all the fluorides have low-damage tolerance.) The repetition rate can affect the appearance as well as the stability of supercontinuum from those materials, which will be discussed in the next section. For some fluorides, which have low damage tolerance supercontinuum was only observed at very low repetition rate, what makes a measurement of the spectrum complicated. This data is not presented here.

5.4 Conversion efficiency

A higher Kerr nonlinearity implies a larger broadening, which agrees with experimental results shown in Figure 14.

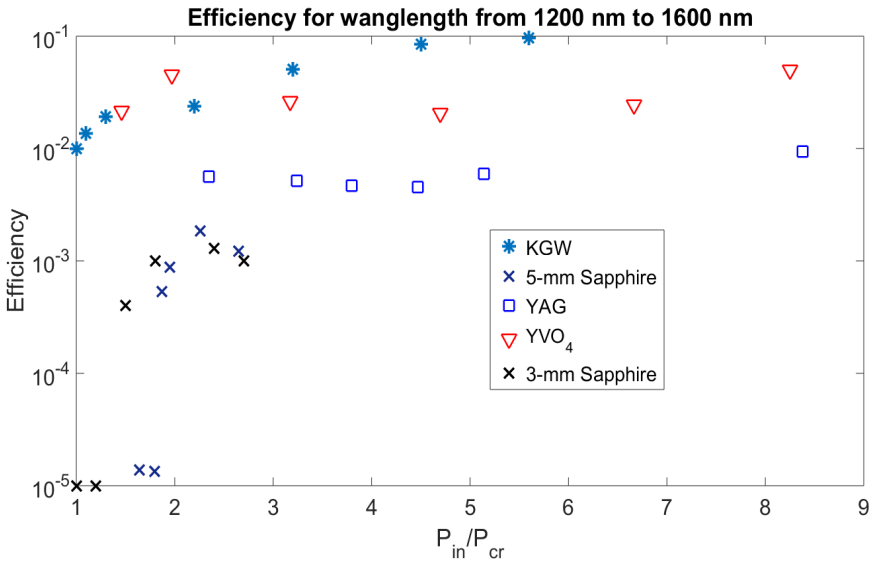

Figure 14: The efficiency of supercontinuum generation in the spectral range 1.2-1.6 μ m plotted against P/P_{cr} in log scale. Different shapes (colors) mark data for different crystals.

From the figure, the spectral broadening through the 5-mm sapphire has higher efficiency than the one of 3-mm, which can consistently with our expectations be attributed to a longer filament supported by a thicker sample. More discussions will be presented in the simulation chapter.

5.5 Laser-induced optical damage

Laser-induced optical damage in our experiment is a big issue for supercontinuum generation. Usually, continuous laser radiations cause damage only at very high power accompanied with significant absorption lines that match the laser wavelength. The laser-induced damage mostly takes place for pulsed lasers [43].

In our case, the laser power is in the scale of MW. After being focused by lenses, the waist size is usually reduced to μm scale, which exhibits enormous laser intensity in sub-TW /cm^2 scale. In addition, the nonlinear processes would further increase the intensity. The laser-induced optical damage can be divided into two sources, single shot damage that is related to every single pulse energy and accumulative damage that is related to the average laser power (both the laser repetition rate and the pulse energy contribute). In every laser shot a certain number of electrons is generated. When those electrons recombine, after the laser pulse has passed, the energy is dissipated as heat. Since the cumulative heat cannot diffuse rapidly enough, the material might overheat at high repetition rate. Cumulative interaction between subsequent pulses might also happen by the accumulation of defects, such as color centers. Those have a lower ionization potential and thus more and more electrons are generated from shot to shot, leading to stronger heating and faster damage. Finally, damage might also happen in a single shot, if the density of generated electrons is large enough to trigger subsequent destructive mechanical effects such as melting, shock, waver, and dissipation [44].

In our experiments, some materials such as fluorides that exhibit very low damage tolerance to the laser repetition rate are also tested. We try to determine and understand the principles of the optical damage in order to avoid such situation as well as to select correct materials for subsequent OPA processes. Here the only judgement for the damage threshold is the observation of a blinking pattern on a white paper or the degradation in supercontinuum spectra under given illumination conditions. The repetition rate can be tuned to any integer divisor of the fundamental repetition rate with the built-in pulse picker. Because the single shot damage can only be determined in a very low laser repetition rate where in our experiment the supercontinuum emission is neither detectable nor observable, only the cumulative damages of different crystals at high repetition are roughly tested.

Table 3 shows some physical parameters of our materials as well as the relative damage thresholds.

	MgF_2	CaF_2	BaF_2	YAG	Fused silica	Sapphire	KDP
Thermal conductivity ($W{\cdot}m^{-1}K^{-1}$)	21[45]	9.71[46]	11.72[47]	14[48]	1.38[49]	23.1[50]	1.9[51]
Heat capacity ($J{\cdot}\ kg{\cdot}\ m^{-1}K^{-1}$)	1003[45]	854[46]	456[47]	590[48]	740[49]	761[50]	No Inf.
Damage threshold (kHz)	1.5	<1	<1	>200	10-15	>200	>200

Table 3: The first two rows indicate thermal conductivities and heat capacities of the tested materials. The experimental optical damages due to the laser repetition rate around critical powers are listed in the third row.

As for the optical damage at 200 kHz, results are listed below.

	YVO_4	KGW	YAG	Fused silica at 10 kHz	Sapphire	KDP
Damage threshold (P_{in}/P_{cr})	>10	>10	>10	2.1	3	3-5

Table 4: The laser-induced damage threshold with respect of the pulse input power

As can be seen in the tables, materials like YAG with large thermal conductivities might have larger diffusion rates to transfer heat efficiently away from the focusing point [43]. Actually, the laser-induced optical damage is much more complicated than the thermal diffusion and to be determined. They can be attributed to a big set of factors such as the avalanche process where the impact-ionization chain leads to a local heating of the material, surface defects that change the dielectric properties of the material, as well as optical quality (purity and fabrication details) [43]. This is why the thermal conductivity alone cannot explain the contradictory behavior for the fluorides compared to YAG and Fused silica.

6 Simulation results

The codes describing the propagation of short pulses in media as well as driving the simulations are written by a French scientist, Arnaud Couairon, from École Polytechnique. The simulation of the propagation is based on the moving focus model assuming that pulse divided into time slices, are independent from each other. The slices carrying certain powers are calculated individually, for example, slices with peak powers above the critical power will focus while others with lower powers will only diffract.

The basic model is the unidirectional nonlinear Schrödinger propagation equation, and the other models involving diffraction, the Kerr effect, Multi-photon excitation (absorption), plasma current density can be viewed as extensions of the basic model. And we tried to investigate each mechanism and the collective effect from all the possible factors of the formation of the laser induced filamentation as well as its related supercontinuum outcome.

The numerical stability of results can be strongly affected by the numerical resolution (step) in both the temporal and spacial domains. The temporal steps are chosen to be 1024 for all the simulations while the spatial steps are usually modified according to practical cases to meet the equilibrium between the elapsed time and numerical stability. For example, intensely illuminated areas such as the self-focusing focuses always require very high spacial resolutions to stabilize the numerical results (The spacial resolution can be modified in any propagation interval). It should be stressed that the numerical stability implies only the precision of the result in stead of its accuracy.

The initial laser pulse for the numerical computation is chosen based on the practical experiment. The unchirped pulse centered at 1030 nm has a Gaussian profile in the temporal domain with pulse duration τ_p=200 fs and pulse energy from 0.5 μJ to 5 μJ. In the spatial domain, we consider a Gaussian beam focused by a lens to a waist diameter of 20 μm. The material mainly used for the simulation is fused silica because of its well-known properties. While parameters, such as dispersion data, refractive index and band gap can usually be obtained for each material, the delayed Raman response is often unknown.

6.1 The effect of self-focusing

We start from the pulse propagation without undergoing any other effect but diffraction in the medium. The result is shown in Figure 15. The red curve marks the beam size at half of the peak intensity.

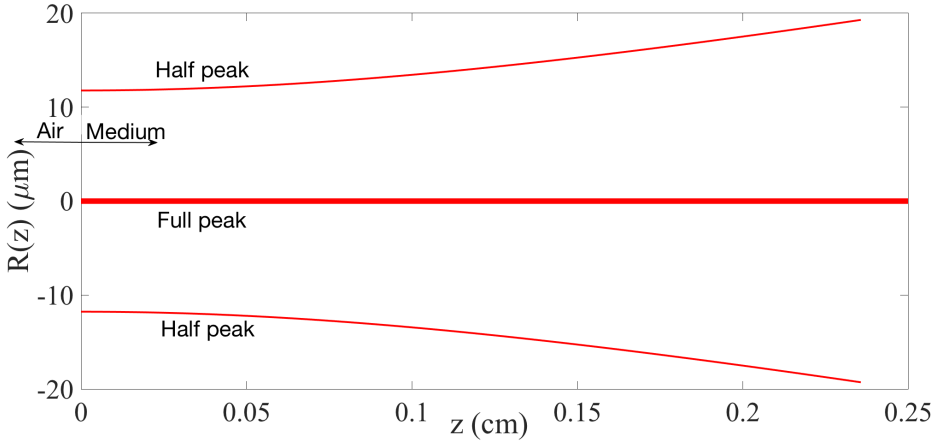

Figure 15: The intensity at the half of the center intensity along the beam path

Diffraction is a basic feature of the wave. Because interference takes place in the boundary of a finite size beam, the beam will always diverge along its propagation path. This manifests in the behavior of the Gaussian beam. In addition, the laser pulse is not monochromatic, so longer frequencies diffract more than shorter frequencies. We now want to investigate the Kerr effect at different input power and compare its self-focusing collapse length to Equation 2.13.

The Kerr nonlinear refractive index of fused silica is $n_2 = 3.2 \cdot 10^{-16}$ cm^2/W (from Table 1), corresponding to a critical power P_{cr}=3.45 MW. The laser energy varies from 0.9 μJ to 2 μJ corresponding to the peak input powers P_{in} between 4.2 MW to 9.3 MW, slightly higher than the critical power. The group velocity delay is derived from the Sellmeier equation. The result is illustrated in Figure 16. It should be noted that the numerical treatment around the collapse point is challenging because the simulation does not deal well with high intensity values. The intensity continues to grow until the collapse is arrested by ionization and plasma defocusing.

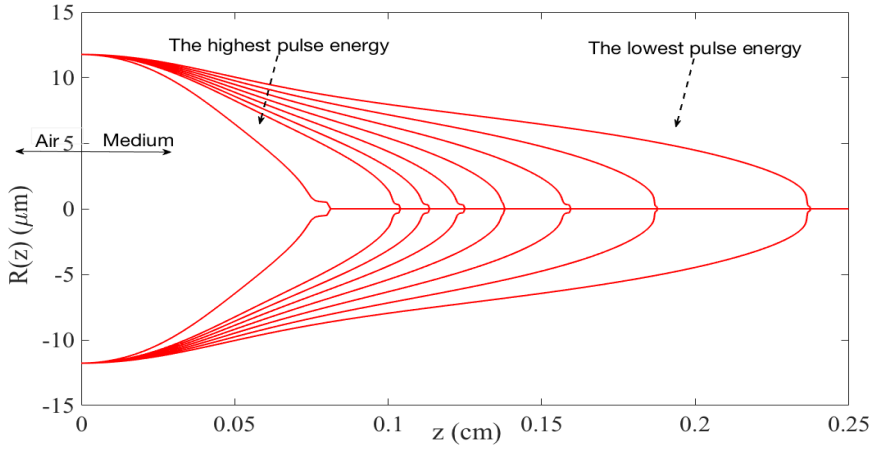

Figure 16: The intensity at the half of the center intensity along the beam path for different input power.

According to Equation 2.13, the collapse length is a function of the ratio P_{in}/P_{cr} and Figure 17 shows the simulated results as well as the collapse lengths.

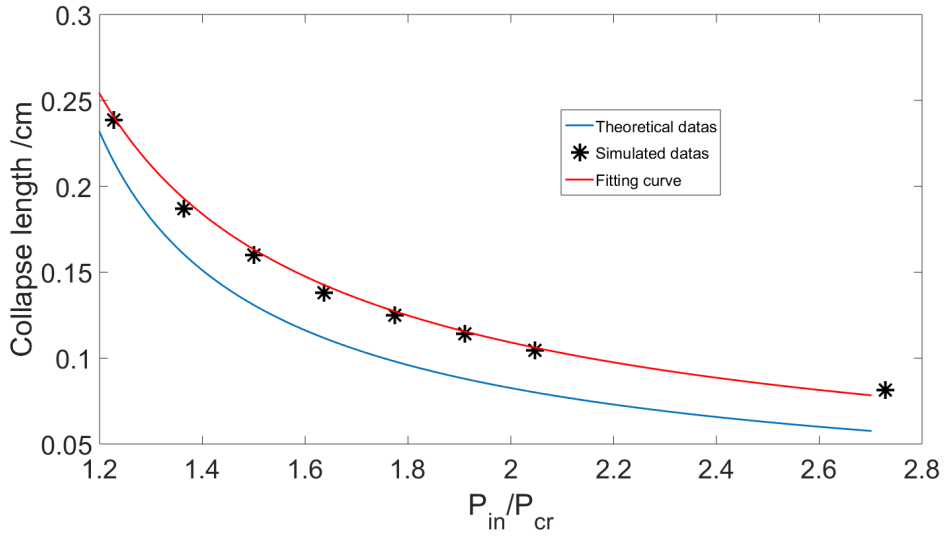

Figure 17: The blue curve shows the theoretical predictions from Equation 2.13. the black stars are the simulated collapse length in Figure 16; the red curve is the new fitting curve for the simulated datas.

The origin of the mismatch between the theoretical and the simulated results is the presence of the group velocity delay. As we know, the group velocity dispersion bends the spectral phase of the transform-limited pulse as well as stretches the pulse in the temporal domain. This effect might lower the pulse peak power resulting in a longer collapse length. Equation 2.13 obtained from a semi-empirical formula is only valid for monochromatic waves [29] [30]. For our input parameters the equation for the collapse length could be modified to

$$L_{cs} = \frac{5.336 z_0}{\sqrt{[(P_{in}/P_{cr})^{0.5} - 0.0.7994]^2 - 0.0219}} \tag{6.1}$$

by fitting to the experimental data. It is worth to stress that such fit is only valid for a given pulse duration and a given material.

6.2 Simulation of the laser induced filament

In this section, the effect of plasma-defocusing is under consideration. Figure 18 illustrates the laser induced filaments in fused silica at different input powers. The oscillatory structures in the trailing part of filaments originate from numerical instabilities.

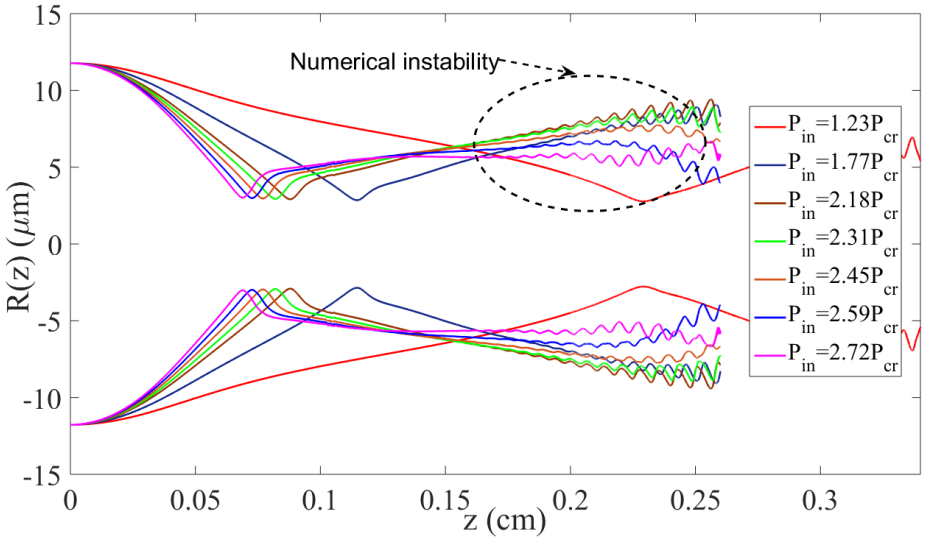

Figure 18: The beam size at the half of the peak intensity along the beam path for different input power

Distances are measured from the entrance to where the beams start to diverge due to plasma defocusing and are compared to L_{cs} in Equation 6.1. Figure 19 illustrates simulated positions of the arrest of collapse from Figure 17.

Due to a rapid plasma generation close to the collapse point, the collapse is arrested before the actual collapse point is reached. Thus, these distances are slightly shorter than what Figure 17 shows.

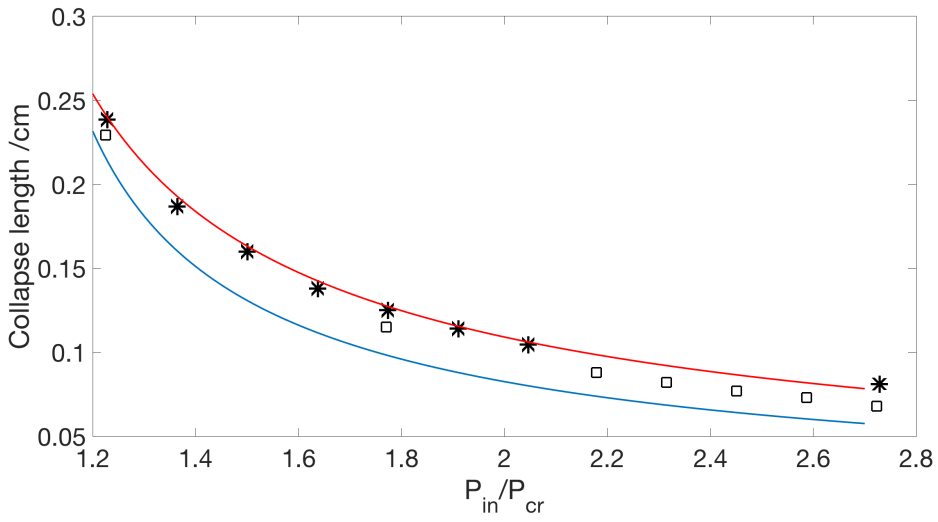

Figure 19: Squares in the graph mark positions where the beams start to diverge. The red curve and blue curve are the theoretical and numerical lengths when plasma-defocusing is absent.

The plasma defocusing is very pronounced close to the collapse point, because the generation of free electrons is proportional to the laser intensity. Close to the collapse point, the ionization rate grows exponentially and plasma defocusing arrests the collapse.

6.2.1 Raman contribution

The interest here is the Raman contribution. We try to evaluate its effect by again looking at the collapse point in Figure 20.

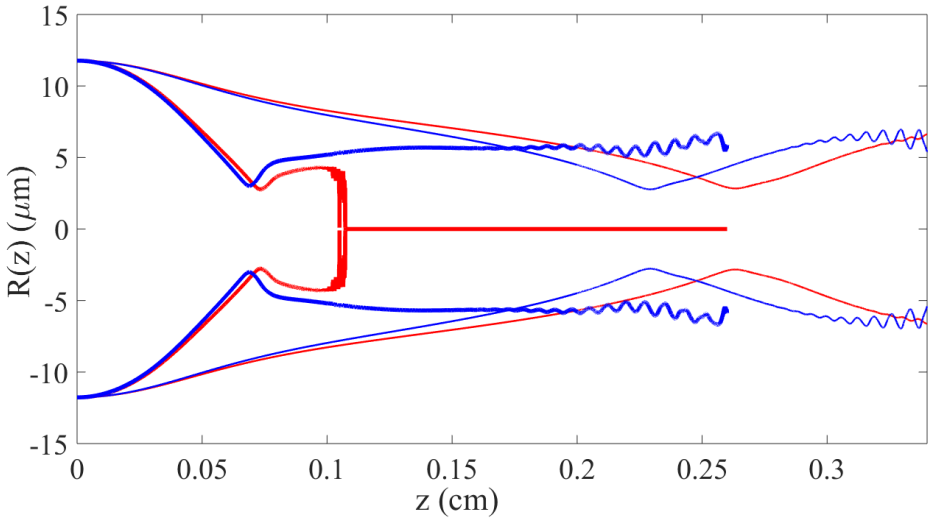

Figure 20: The input pulse powers are $P_{in} = 1.23P_{cr}$ (thin lines) and $P_{in} = 2.72P_{cr}$ (thick lines). Blue and red color indicate the instantaneous and delayed Kerr effects, respectively.

From Equation 2.26, the Raman response of the molecular vibration results in a partial delay of the nonlinear response which leads to effectively reduced self-focusing. Consequently, the position of the self-focusing collapse is also moved backward by the Raman response.

6.2.2 Plasma density due to ionization

Figure 21 illustrates the instantaneous maximum electron density in the spatial domain along the beam path as well as in the temporal domain for a pulse with $P_{in} = 2.72P_{cr}$.

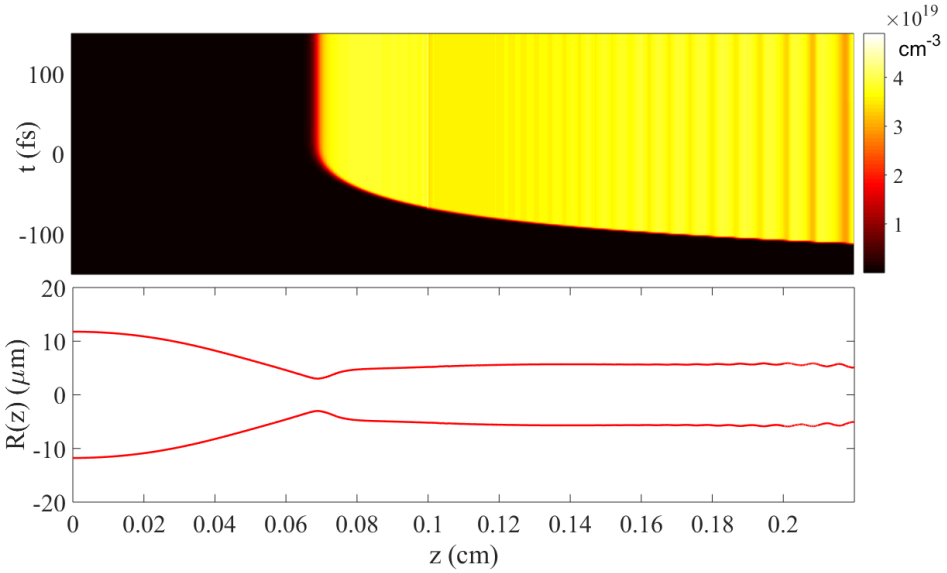

Figure 21: The figure on the top shows the highest instantaneous electron density in time and space. The figure on the bottom shows the beam size at half of the peak intensity.

It is obvious from the figure that plasma defocusing balances self-focusing only at the high electron density from where the filament starts. Two slices in time are shown in Figure 22.

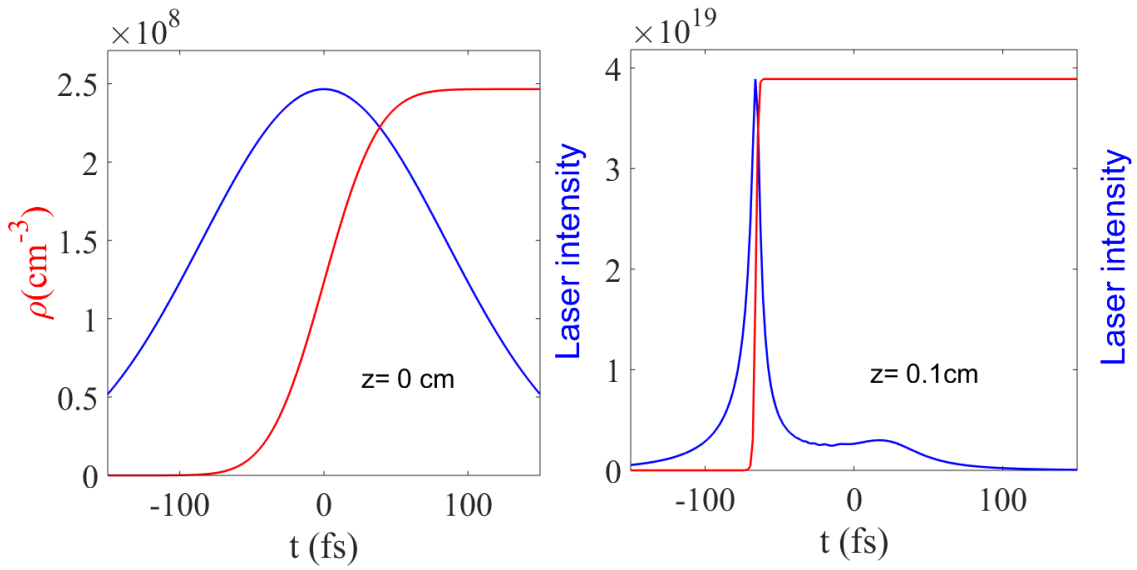

Figure 22: Temporal pulse profile (blue) and plasma density (red) at two different distances during propagation

The electron density increases enormously with the pulse power near the peak and accumulates to a large amount in the trailing part of the pulse. Because the electron (plasma) generation rate increases exponentially with laser intensity, the plasma effect is much more dramatic for shorter pulses, or at the collapse of self-focusing, as well as

in the filament. Here, electron-ion recombination and nonlinear losses are not taken into account (They are considered later).

6.2.3 Evolution of the laser pulse

In the temporal domain, the filament acts as a pulse compressor since new frequencies are generated in the filament, which can widen the spectrum. This can result in shorter pulse duration. The processes are illustrated in Figure 23.

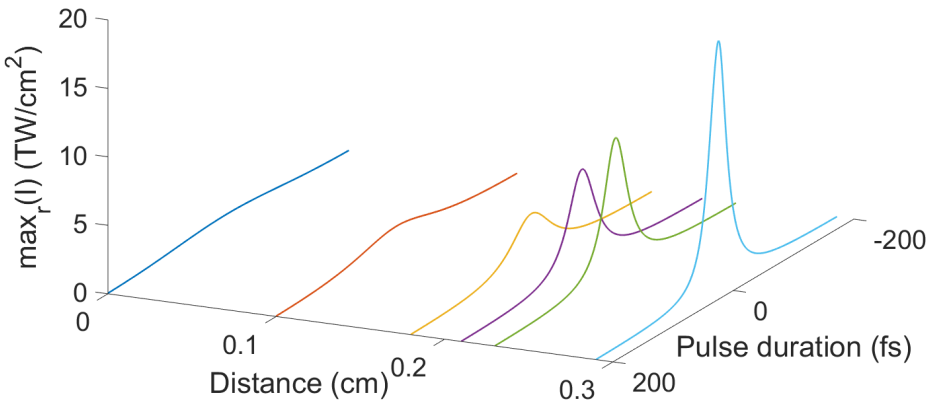

Figure 23: The laser input power is $P_{in} = 1.23P_{cr}$. Evolution of the temporal profile. The temporal profile is plotted at different propagation distances in the material.

.

At very high power in a dispersive medium, the spectrum might become very broad and structured. Under the effect of dispersion, different spectral components have different group velocities and the pulse can be ripped apart into two or more pulses, as shown in Figure 24. In fact, the pulse splitting can also be attributed to the interplay between self-focusing and plasma-defocusing in the spatial-temporal domain which will be discussed later.

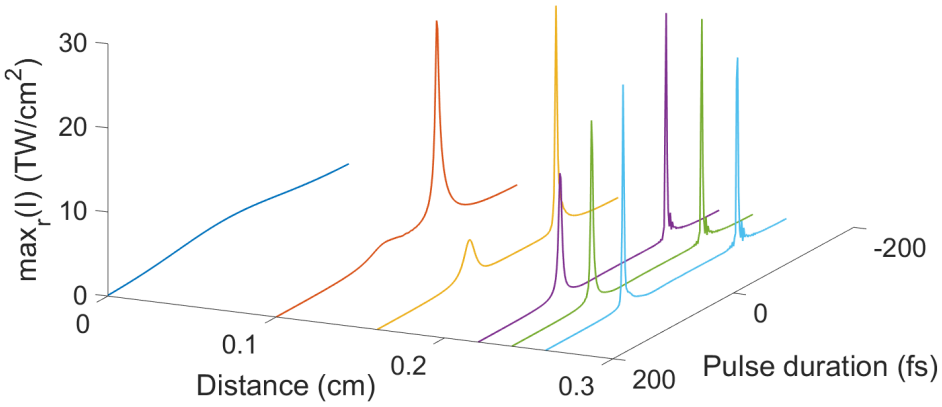

Figure 24: The laser input power is $P_{in} = 2.72P_{cr}$. Evolution of the temporal profile. The temporal profile is plotted at different propagation distances in the material.

.

The evolution of the pulse splitting with the input power is illustrated in Figure 25.

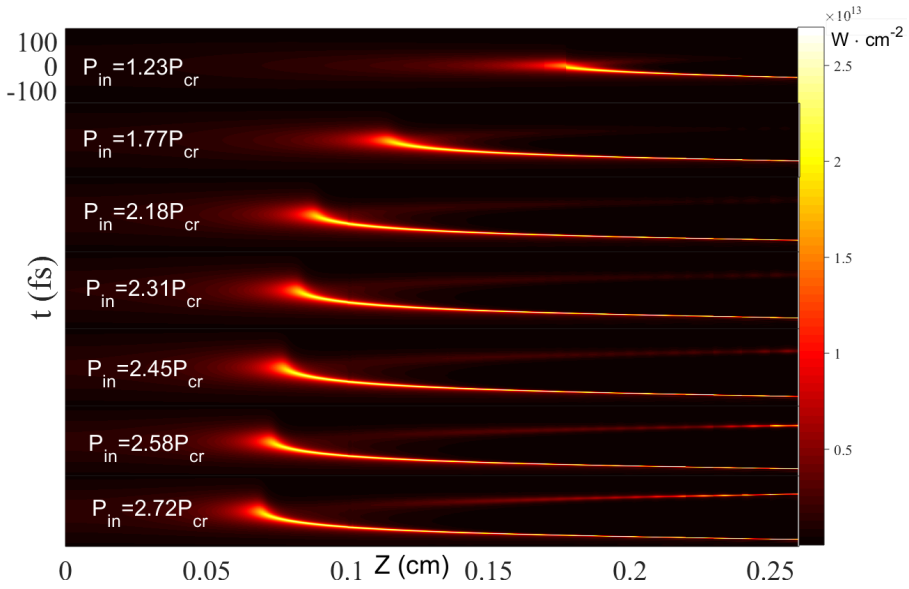

Figure 25: 2D color map plot of the intensity as well as propagation distance for different input powers.

The pulse intensities are presented by a 2D color map. The weaker tails on the upper part of each map are the pulses split from the original pulses. It is very clear that the pulse splitting effect strengthens with the input power. The splitting should be understood as a result of the complicated interplay of several nonlinear effects. Also multi-photon absorption may have a prominent role here.A comparison is shown in Figure 26, when the absorption is introduced in the top plot.

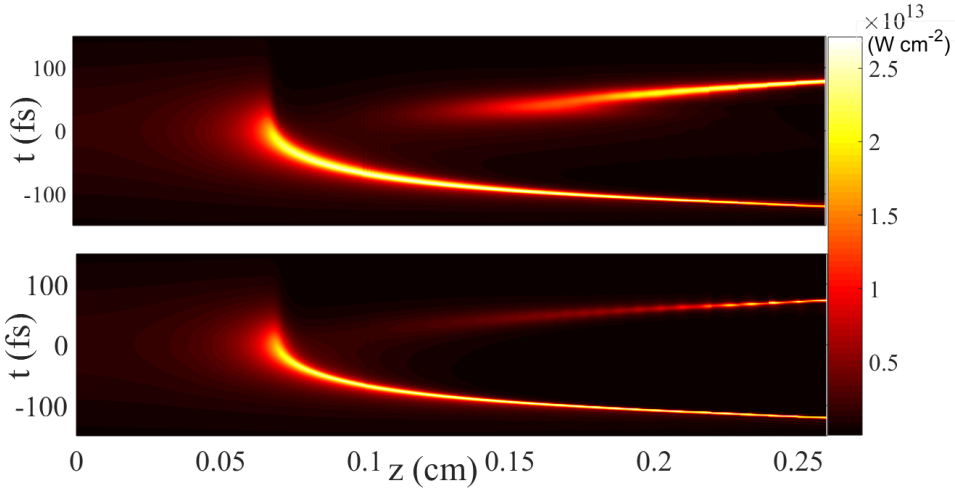

Figure 26: The input power is $P_{in} = 2.72P_{cr}$. The figure on the bottom is the last graph of Figure 25 and the figure on the top is obtained with same condition but here the absorption is introduced.

As can be seen from the graph, the splitting effect is much stronger when the absorp-

tion is present.

6.2.4 Nonlinear losses and electron-ion recombination

In addition, regarding to the imaginary part of Drude model (Equation 2.21), the rate of plasma absorption and multi-photon absorption are always synchronous with the multi-photon excitation that generates free electrons. As can be seen in Figure 27, the integrated pulse energy has a sharp drop after the arrest of the collapse due to nonlinear losses.

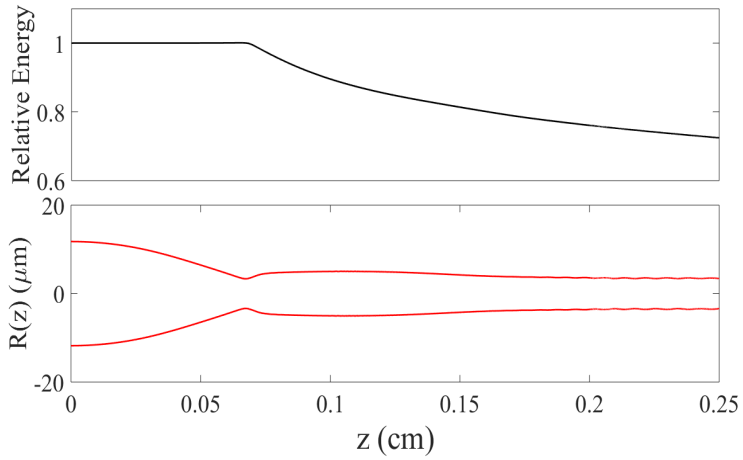

Figure 27: The red curve is the beam size at the half of peak intensity, the black curve is the integrated energy along the transverse plane.

As the electron-ion recombination is introduced, the electron density is effectively attenuated, as shown in Figure 28.

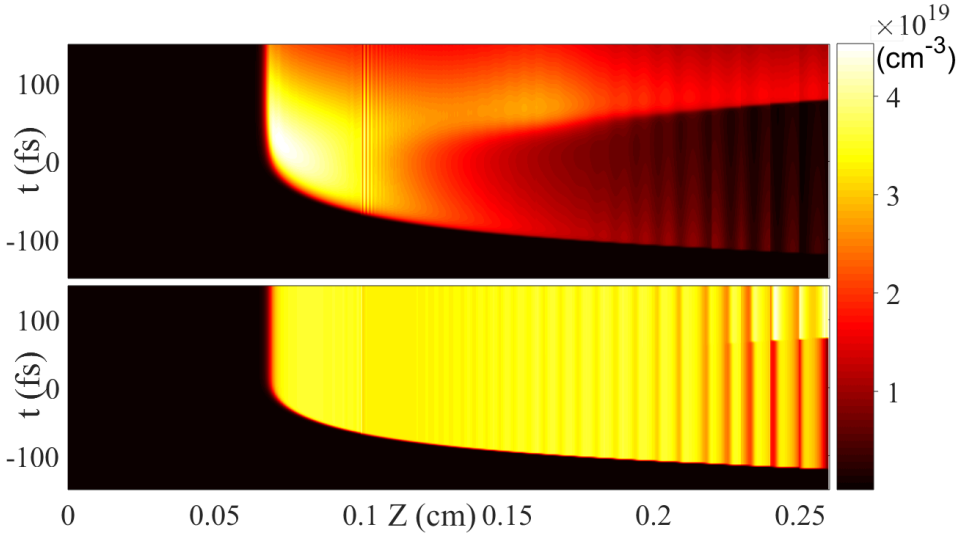

Figure 28: The figure on the bottom is the one in Figure 22 obtained with input power $P_{in} = 2.72P_{cr}$. The figure on the top is obtained, including electron-ion recombination.

As can be seen, the recombination reduces the overall electron density especially after the first pulse. It should be noted that photons emitted from recombination are not taken into account in the simulation, nor do they contribute much to the results. The photons from recombination happening on much slower time scale are neither coherent nor directional.

6.3 Supercontinuum emission

The spectral broadening accompanying laser induced filamentation is strongly dependent on the temporal redistribution of the pulse. In this stage, the coupling effects consist of diffraction, self-focusing, self-phase modulation, self-steepening and nonlinear ionization. Figure 29 illustrates the supercontinuum spectrum in some positions along the medium.

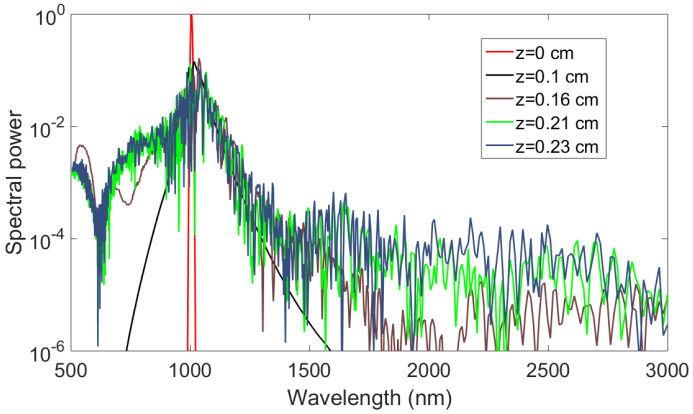

Figure 29: On-axis spectra obtained in fused silica at different positions inside the sample. The laser input power is $P_{in} = 2.72P_{cr}$.

.

For convenience, the spectral broadening above 3000 nm is not presented, since we are only interested in a shorter wavelength regime. As can be seen, the spectral broadening increases and accumulates with propagation distance. After the collapse, the broadening is becoming dramatic, because the self-steepening as well as plasma defocusing introduce new frequencies in the UV regime. Usually, self-phase modulation should lead to symmetrical broadening both to the blue and the red side. However, the symmetry is broken by plasma generation and self-steepening, usually making the trailing edge of the pulse much steeper, leading to stronger broadening to the blue than to the red side. Figure 30 shows more details of the spectral broadening along the propagation including the radial emission.

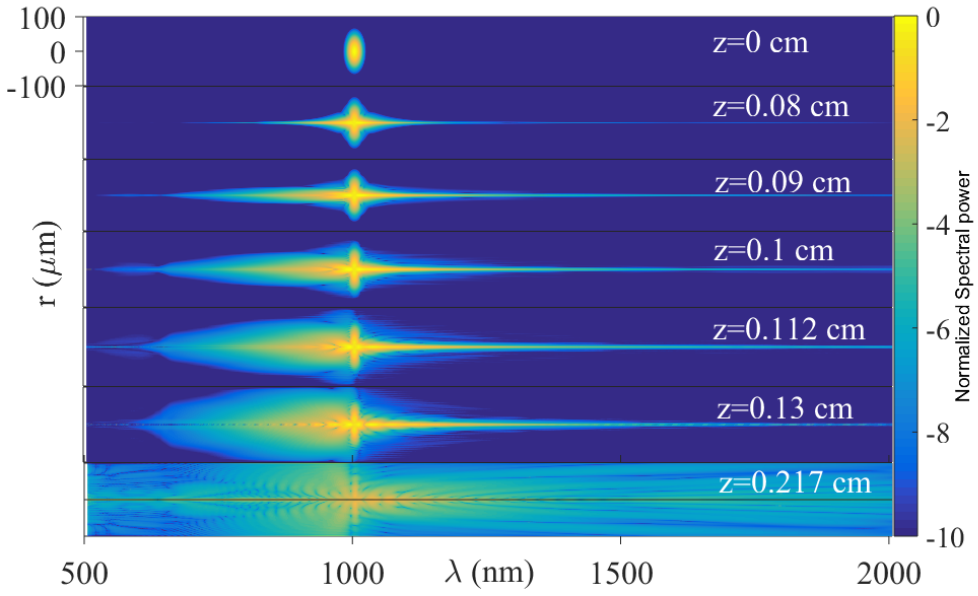

Figure 30: The evolution of the spectrum in the medium. All the spectral powers have been normalized. The color scale is logarithmic.

.

Before the collapse which is around 0.075 cm from the entrance, the broadening is symmetric due to self-phase modulation. Then the broadening towards the UV regime becomes significant by the arrest of the collapse due to plasma defocusing. Further down the propagation, the low power parts of the pulse, which do not carry enough power in time and space, diverge to form the radial emission of broad band continuum. Figure 31 illustrates the corresponding temporal profiles.

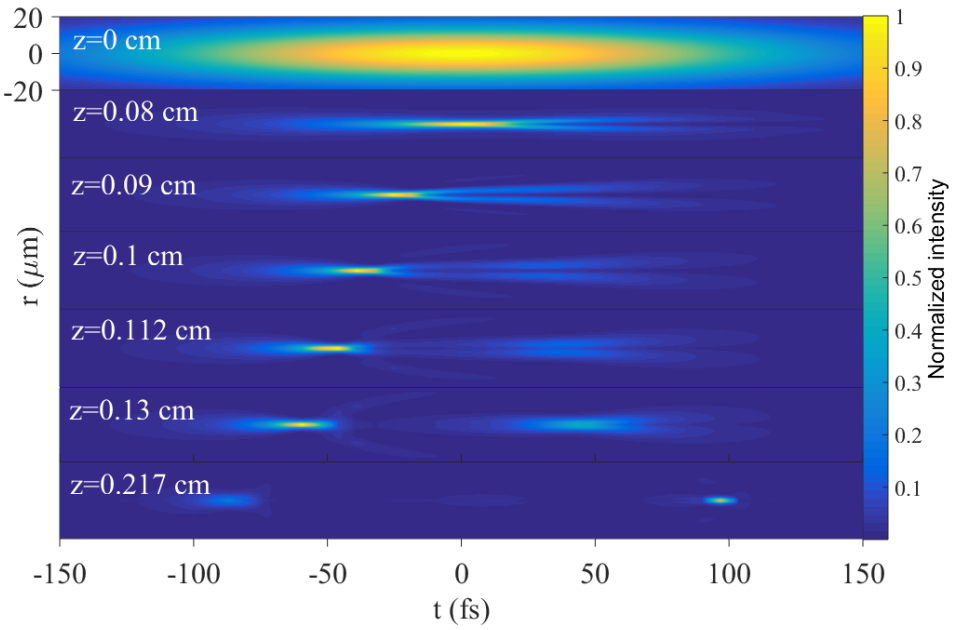

Figure 31: The evolution of the pulse in the medium.

.

The pulse undergoes spatial and temporal compression as it transmits. As shown in the figure, self-focusing leads to an increase of intensity until the arrest of the collapse. At a certain level of nonlinear ionization, plasma generated in the leading half of the pulse defocuses the trailing half. The higher the intensity grows, the earlier in time this point moves. The trailing edge that had been pushed away from the optical axis may refocus due to the Kerr effect, as shown for z=0.13 cm.

6.3.1 Supercontinuum from Sapphire and YAG

In this stage, we want to investigate the simulated supercontinuum from different materials. The simulations are based on the physical parameters from Table 1 and Figure 32 illustrates the induced filaments in Fused silica, Sapphire and YAG. As can be seen, the collapse lengths around 0.12 cm are well-predicted by the fitting curve in Figure 19 (red). The slight difference in collapse lengths for them can be due to very complicated and competitive dynamics between self-focusing as well as plasma defocusing that depends on the band gap.

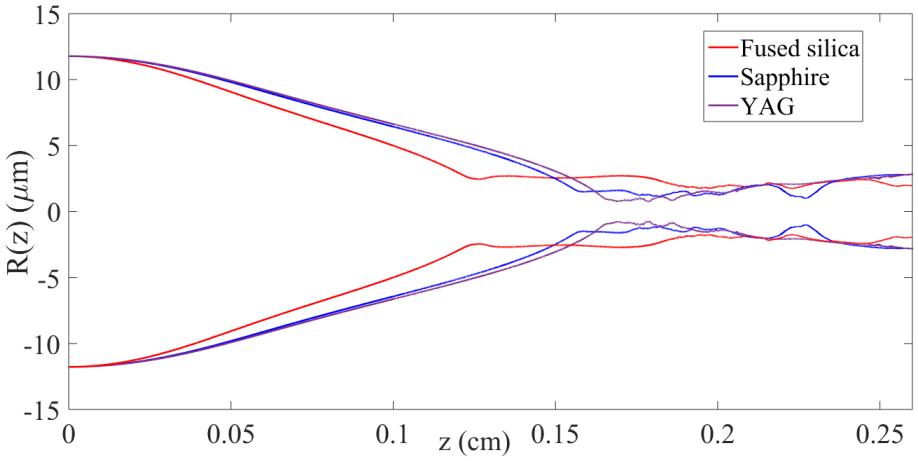

Figure 32: Filaments induced by the input power P_{in}=1.77P_{cr} for three materials.

.

The corresponding spectra are shown in Figure 33. The results show that the YAG crystal with the highest nonlinearity has the largest broadening.

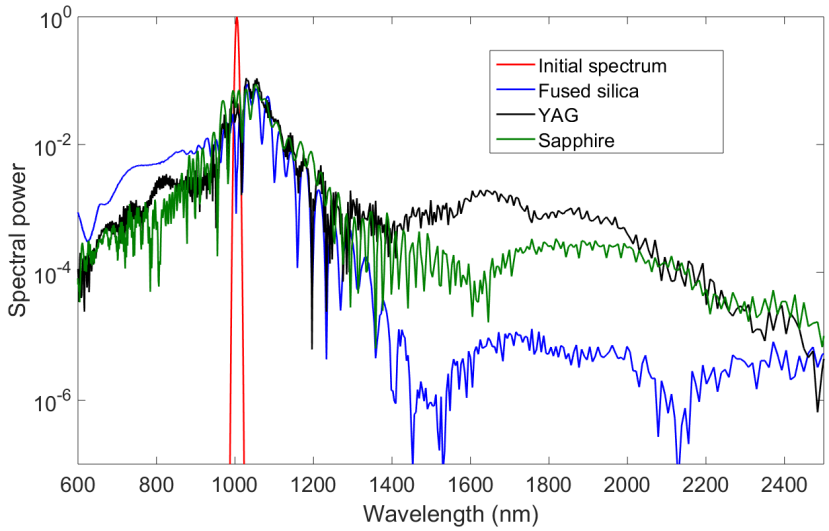

Figure 33: At a distance z=0.25 cm, supercontinuum from Fused silica, Sapphire and YAG are shown.

.

6.3.2 Impact in supercontinuum generation by focusing conditions

As can be seen in Equation 5.1 the waist size is only determined by the use of the lens as well as the original beam size. All the simulations above are based on incident beams at the Gaussian waist. But in the practical experiment, it is impossible to define the position of the waist without help of precise instruments since the beam size at the focus varies on micro-meter scale (see Figure 34).

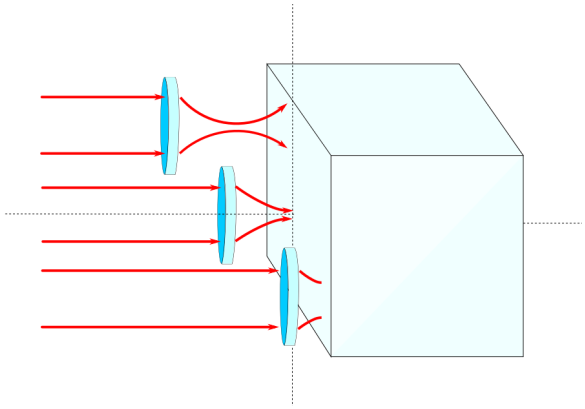

Figure 34: In reality, crystal surfaces usually somehow mismatch the focus of lens, which may result in total different supercontinuum spectra.

.

In this stage, we want to investigate how the position of the lens focus impacts the output supercontinuum in a certain size material by simulating practical cases that might exist. Beams will not be incident at the waist now. Figure 35 illustrates the beam size as a function of propagation distance before simulations.

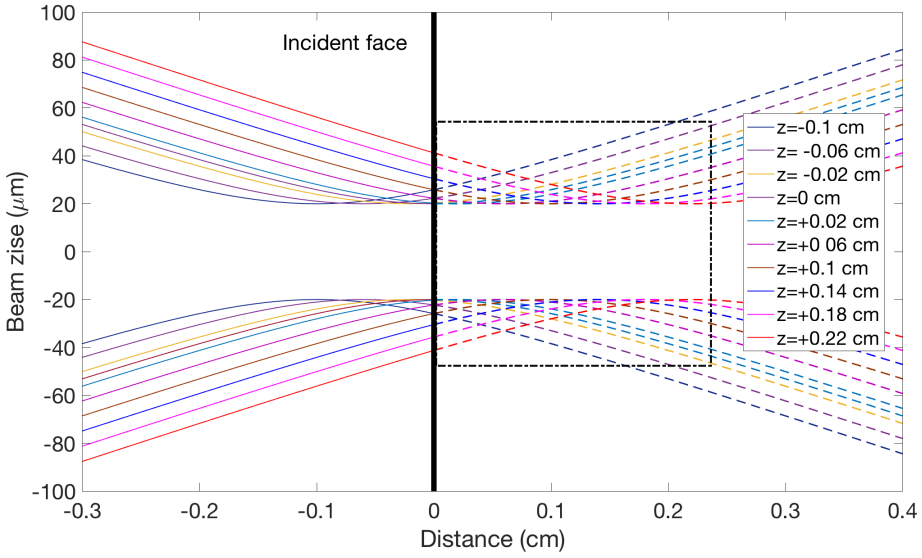

Figure 35: The waist size is still 20 μm but may not be located at the incident plane. Different colors indicate the waist positions (before or after the incident face). The dotted lines illustrate the original beam tracks without any medium. z here is the position of the waist with respect to the position of the crystal ('+' imply positions inside the crystal and '-' imply positions before the crystal surface.).

.

We begin with simulations of filaments taking into account focusing conditions as illustrated in Figure 35. Results are illustrated in Figure 36. It should be noted that curves in Figure 35 are Gaussian beam size at $1/e^2$ of the peak intensities and in Figure 36 are beam size at half of the peak intensities as used before.

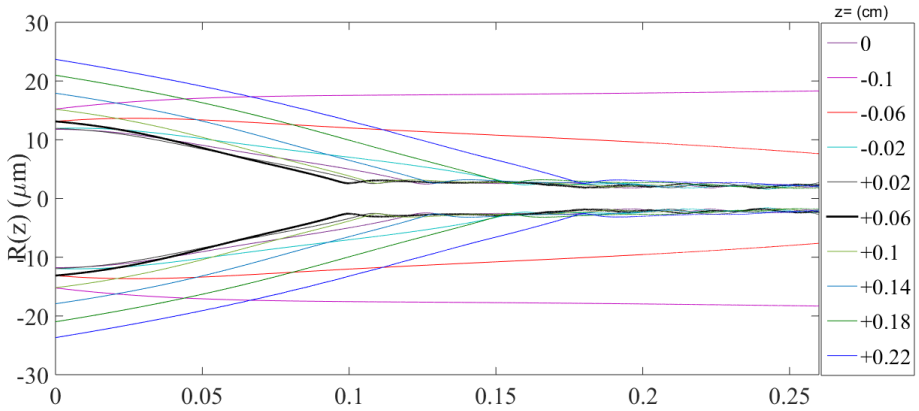

Figure 36: The solid lines are beam sizes at different input waist positions when the medium (fused silica) is present. The shortest collapse track is marked by the bold black curve when z=0.06 cm.

.

The shortest collapse track is marked by the bold black curve when z=0.06 cm instead of z=0 which is for a collimated beam. As we know, the radius of curvature of a Gaussian beam increases with the beam size. The convergence angle given by an increase in the radius of curvature tends to shorten the collapse distance. Meanwhile, the increase in beam size lengthens it. This competition is optimized for the shortest collapse length when the convergence angle is slightly above zero. In this case, at z=0.6 the radius of curvature is R=-0.3089 cm. More details are illustrated in Figure 37.

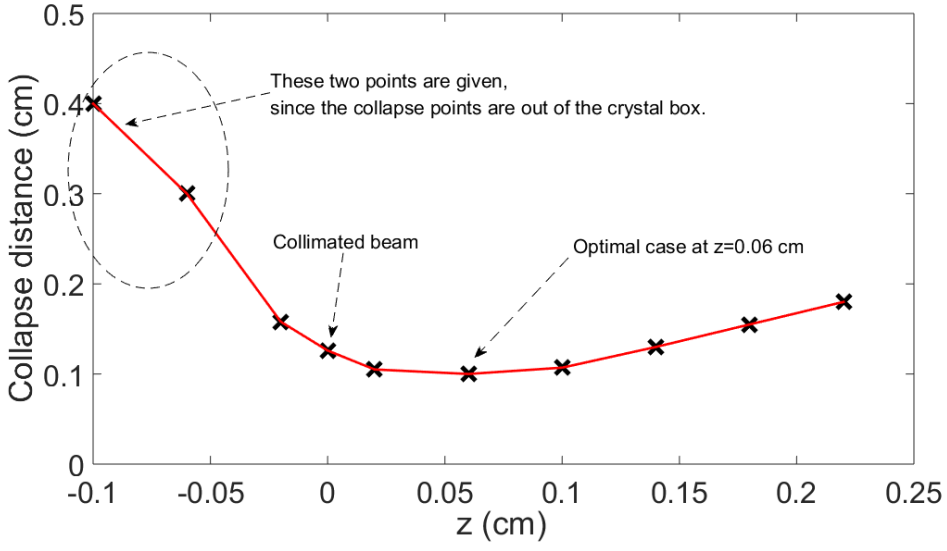

Figure 37: The collapse distance as a function of the position of the waist. The first two spots are 'guessed' because they are not in the numerical box.

.

The waist position is important because a shorter collapse length allows a longer filament in a certain length medium as well as improves the efficiency of supercontinuum

generation. The spectral broadening as a function of the waist position is illustrated in Figure 38.

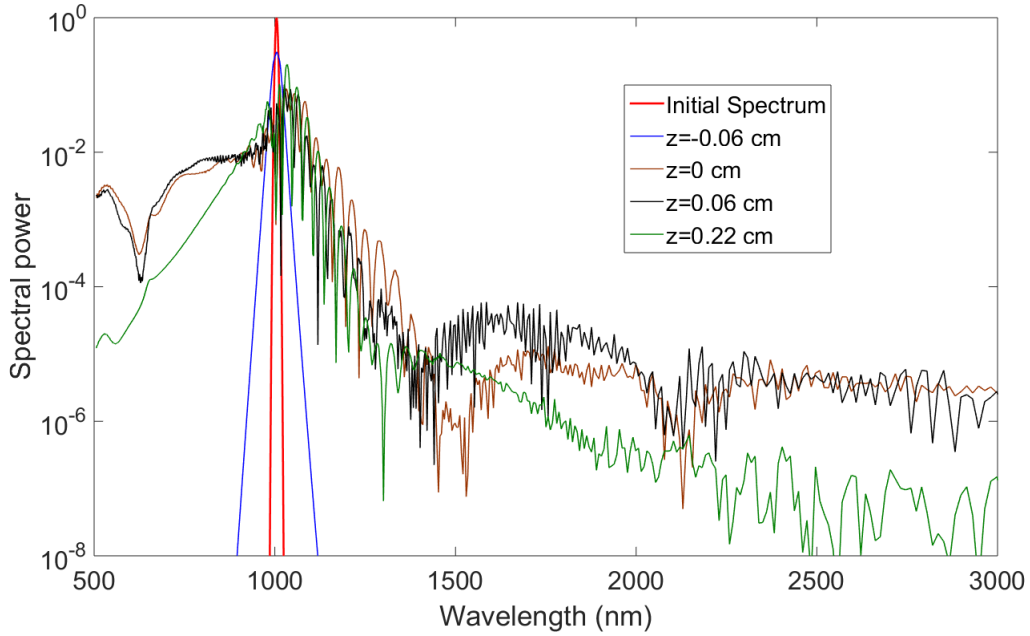

Figure 38: The black curve (z=0.06 cm) has stronger spectral power (1400 to 2000 nm) compared to the brown curve, which can be attributed to a shorter collapse distance.

.

7 Dispersion scan outlook

In this section, we quickly discuss a technique to characterize the temporal profile of the generated supercontinuum. The approach was planned and a set was designed, but due to a lack of time no measurements were performed. A pulse can be fully described by the Fourier transform of the complex spectral envelop $V(\nu)$, consisting of a spectral power $|V(\nu)|^2$ and a spectral phase $\phi(\nu) = \arg(V(\nu))$—a shorter pulse duration is obtained with larger bandwidth of the spectral power as well as flatter spectral phase. In order to characterize the spectral phase of the supercontinuum, the dispersion scan (D-scan) technique can be introduced [52]. D-scan technique has been found since 2012 by Miguel Miranda. This method is very similar to a well-known technique called multiphoton intrapulse interference phase scan (MIIPS) [53].

The basic idea is that known spectral phases are applied to an unknown pulse and the resulting second harmonic generation (SHG) signal is measured. Scanning the well-known spectral phase results in 2-D D-scan graphs. The initial spectral phase can be retrieved by minimizing the error between a measured and a simulated D-scan trace [54].

Suppose a laser pulse described by a complex spectral amplitude $A(\nu - \nu_0)$ centered at ν_0, where $|A(\nu - \nu_0)|$ is the square root of the spectral power and $\arg(A(\nu - \nu_0))$ is the spectral phase. Suppose an additional spectral phase ϕ_0 introduced by optical elements. To perform a D-scan, A phase $2\pi\nu n_{no}(\nu)l/c$ is introduced by a normal dispersive medium, and $2\pi\nu n_{an}(\nu)z/c$ is introduced by an anomalous dispersive medium, where $n_{no}(\nu)$ and $n_{an}(\nu)$ are the refractive indices approximated by Sellmeier equations. z and l are the effective length of the two media. The spectral power $D(\nu, z)$ of the second harmonics is derived as

$$D(\nu, z, l) = |\mathscr{F}\{[\mathscr{F}^{-1}\{A(\nu - \nu_0)\exp(-i\phi_0 - i\frac{2\pi\nu}{c}n_{no}(\nu)l - i\frac{2\pi\nu}{c}n_{an}(\nu)z\}]^2\}|^2 \quad (7.1)$$

where $\mathscr{F}$ and $\mathscr{F}^{-1}$ denote the Fourier transform operator and inverse Fourier transform operator, respectively [52].

The tunable length can be realized by the use of a prism pair since the effective length is dependent on the insertion of one prism, as illustrated in Figure 39.

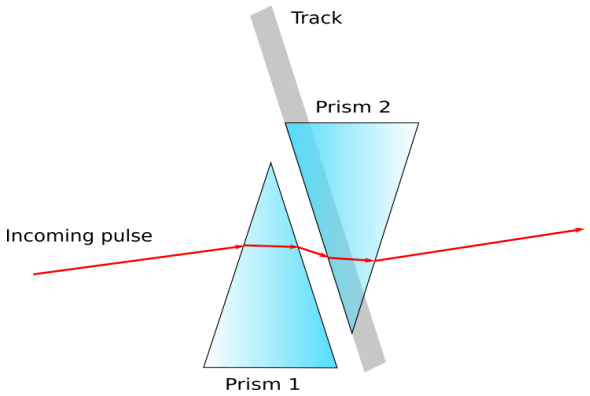

Figure 39: Schematic diagram for dispersion scanning. Prism 2 can be motorized along the indicated track in order to scan the effective dispersion.

In fact, only one of the two effective lengths (either l or z) is necessary to be scanned, while the other one can be fixed at certain position to ensure that the D-scan is performed

around the transform limit. In this case, both determination of the spectral phase and compression of the supercontinuum pulse are realized. The arrangement of normal and anomalous dispersive prisms must have sufficient flexibility to also adapt to materials with an extreme dispersion used for supercontinuum generation, such as YVO_4 and KDP. Several options of the uses of dispersive materials are shown in Table 5 (Datas from RefractiveIndex.INFO).

Wavelength	YVO_4	KDP	SF10	SF11	SF14	Fused silica	BK7
1400 nm	120	-86	47	60	63	-11	7.7
1500 nm	100	-116	33	44	49	-22	-18.6
1600 nm	78	no Inf.	18	18	34	-34	-31

Table 5: GVD coefficients in interesting range of nonlinear crystals and scanning prisms. The unit is fs^2 /mm.

For our experiment, BK7 and SF11 prism pairs will be chosen to perform D-scans. An example of a D-scan graph by scanning the insertion of SF11 prism is shown in Figure 40.

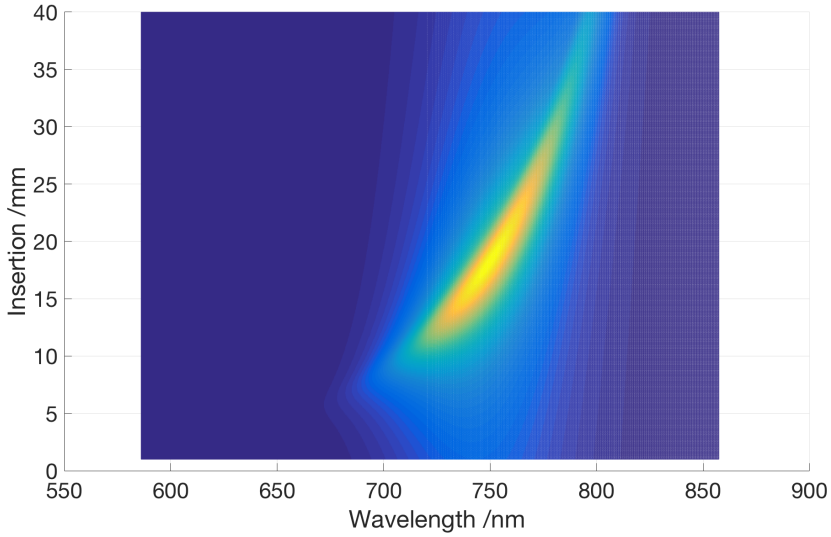

Figure 40: D(λ, z) graph. The input transform limited pulse centered at 1500 nm has a bandwidth of 200 nm and is dispersed by 5-mm KDP crystal.

In order to retrieve the spectral phase of $A(\nu - \nu_0)$, a guessed spectral phase curve $\phi_{gs,n}$ determined by a Fourier series is applied to the spectral power $|A(\nu-\nu_0)|^2$ which has been measured by the spectrometer (n denotes the number of the guessed phase curves). Then, a set of simulated D-scan graphs $D_{sim,n}(\nu, z)$ can be obtained. A merit function is applied to evaluate the difference between the experimental result D_m and a simulated result, shown by Equation 7.2 [54].

$$G_n = \sqrt{\frac{1}{N_i N_j} \sum_{i,j} (D_m(\nu_i, z_j) - \mu D_{sim,n}(\nu_i, z_j))^2} \tag{7.2}$$

where μ is a factor to minimize the error. μ is given by

$$\mu = \frac{\sum_{i,j} D_m(\nu_i, z_j) D_{sim,n}(\nu_i, z_j)}{\sum_{i,j} S_{sim,n}(\nu_i, z_j)^2} [54]. \tag{7.3}$$

With this diagnostics, the experimental spectral phase can be seen as the simulated phase $\phi_{gs,n}$ of which the merit index G_n approaches the minimum.

7.1 Setup

The setup for Dispersion-scan is shown in Figure 41.

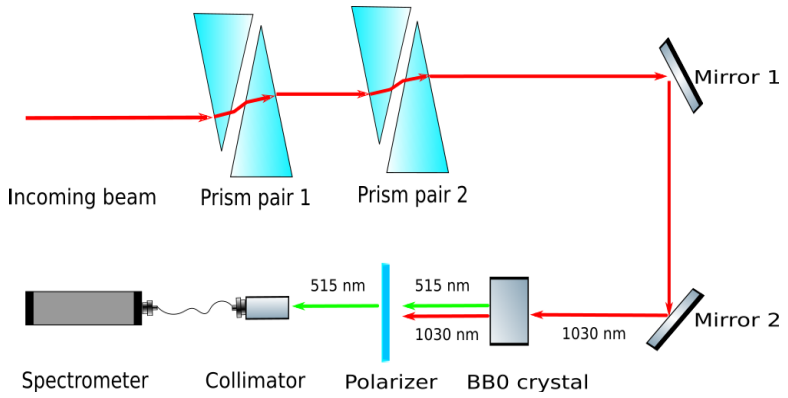

Figure 41: The primary experimental setup for Dispersion scan

One of the BK7 prisms should be mounted on a motorized translation stage in order to allow scanning of the anomalous dispersion of BK7 against the normal dispersion of the subsequent SF11 prisms. For the second prism pair, one of the SF11 prisms should be mounted on a manual translation stage to adapt to incoming pulses with varying dispersion. After the frequency doubling crystal BBO, the fundamental pulse is filtered out with a linear polarizer, since the polarization of the fundamental beam and the second harmonics are orthogonal. The second harmonics beam is captured with a collimator connected to the spectrometer, while the dispersion is scanned by translating the motorized BK7 prism.

8 Outlook

The main goal of this thesis has been to efficiently generate a white-light seed around 1.5 μm wavelength for the possible seeding of a mid-infrared, ultrashort pulse optical parametric chirped pulse amplifier. This has been achieved by focusing intense laser pulses at a carrier wavelength of 1030 nm (PHAROS, Light Conversion) into a number of different material samples. A complex interplay of competing nonlinear effects, such as self-focusing, self-phase modulation, ionization and plasma defocusing, leads to strong spatial and temporal reshaping of the input laser pulses accompanied by a self-channeling effect (filamentation) and massive spectral broadening, termed supercontinuum generation. Whereas spectral broadening towards higher frequencies (shorter wavelengths) is usually straight-forwardly achieved, the challenge in this work has been to obtain strong broadening to lower frequencies (longer wavelengths) as well. A large number of materials have been investigated to find the minimum input power for achieving spectral broadening, to characterize the generated supercontinuum and to evaluate the damage threshold and the damage tolerance.

We have tested around ten different crystals, including sapphire, fused silica, different fluorides (CaF, BaF, MgF) as well as more exotic materials, such as YAG, KGW, KDP and YVO_4. Our experimental results indicate that those more exotic materials are the most suitable for supercontinuum generation with high efficiency for spectral broadening towards the infrared and high tolerance to damage. Similar experimental findings have been reported for YAG [55] as well as KGW and YVO_4 [27]. The results are somewhat surprising since these materials generally have higher nonlinearity and lower bandgap than for example sapphire and fused silica. On the first glance, this should lead to stronger self-focusing, higher peak intensity and due to the low bandgap rapid damage from multi-photon ionization. In our experiments, also KDP performed well for the spectral broadening, but exhibits slightly lower tolerance to damage. KDP is interesting because it changes the sign of dispersion (from normal to anomalous) slightly below 1 μm. This could potentially result in a totally different nonlinear propagation dynamics, which has however not been studied in detail in the current work. To our knowledge KDP has not been used for the purpose of IR (infrared) white-light generation before.From the experimental simplicity point of view, the fact that KDP is hydrophilic might require a sophisticated experimental environment, such as a dry atmosphere or permanent heating, for long term use. Fused silica in our experiment exhibits low damage tolerance. The supercontinuum emission from fused silica usually degrades rapidly at high repetition rate (>20 kHz). The life time for degradation depends on both the pulse energy as well as the laser repetition rate. Life time varying from 2 seconds to several minutes has been reported with the use of an identical laser system [56]. In our experiments the supercontinuum emission from fused silica is relatively stable at repetition rate below 15 kHz and spans up to 1.5 μm. In order to generate this stable supercontinuum at high repetition rate, the cumulative damage could be avoided by dynamically moving the crystal in respect to the beam propagation path. Sapphire is an economic solution for the supercontinuum generation since it exhibits wide spectral broadening and relatively high damage threshold. As for all the fluorides, the reason for the low damage threshold is still not well-known. The mechanisms of optical damage in MgF_2 by femtosecond pump pulses due to both multiphoton ionization and avalanche processes have been reported

[57]. For repetition rates below 1 kHz weak visible supercontinuum was observable by eye, but measuring such spectrum with a scanning optical spectrum analyzer is not possible. For our purpose of generating intense IR white-light at high repetition rate fluorides seem not to be suited.

For a future experimental setup with which possibly also the weak supercontinuum from different fluorides could be characterized, we suggest the following improvements:

- A high-precision translation stage could be applied to position the beam waist in respect to the entrance to the material, since a tiny mismatch of the waist might decreases the output efficiency substantially, as indicated in Figure 36.
- The cumulative damage (not the single shot damage) of materials can be reduced wiggling the material sample in respect to the incoming beam.

As for laser induced optical damage, only rough ideas have been obtained as can be seen in Table 3 and Table 4, because all the results are given by subjective judgements. The subjective judgement is likely making big mistakes when observing the blinking at weak radiation power. For fluorides those blinking emissions at hundreds of Hz are hard to recognize. The blinking phenomenon, which is related to scattering from a possible damage spot, should be understood as practical observation in the study of damage not as scientifically hard criteria. Furthermore, the material alteration can be temporary or even imperceptible [43]. The most appropriate method to investigate optical damage morphology is with a microscope. Apart from that, time resolved digital holography provides direct observations of the optical damage [58].

To get more insight into the different nonlinear effects leading to supercontinuum generation, we also performed numerical simulations based on a Schrödinger-type nonlinear pulse propagation equation [10]. By subsequently switching on different nonlinear effects we were able to qualitatively understand their impact on the nonlinear propagation inside the materials and on the supercontinuum generation. The simulations are in fair agreement with our experimental findings. Quantitative comparison is however not possible since parameters, such as the delayed Raman response of the different materials is typically only known accurately for fused silica due to its huge importance in fiber optics. Still, we were able to show also numerically that the supercontinuum generation in YAG indeed is more efficient than for fused silica. This to our knowledge is the first theoretical attempt to understand why a low bandgap material seems to be better suited for supercontinuum generation to the IR spectral range than high bandgap materials. The exact reasons, i.e. the interplay between different nonlinear effects leading to stronger supercontinuum at 1.5 μm for YAG as compared to fused silica will require further detailed numerical investigations. Furthermore, the numerical model at this point cannot provide insight in the damage mechanisms, since only single-shot interaction between a laser pulse and a material has been considered (can be our future works).

Finally, we look forward to characterizing the obtained supercontinuum with the D-scan technique. Only if the spectral phase of the supercontinuum is well behaved in the interval of interest, i.e. 1.4 – 1.5 μm, the pulse can be temporally compressed close to the transform limit. Recently, a white-light seeded OPCPA (Optical Parametric Chirped-pulse Amplification) very close to our ideas has been presented by a French research group [59], indicating that the nonlinear phenomena investigated in this thesis indeed can be used for seeding mid-infrared OPCPAs (Optical Parametric Chirped-pulse Amplifiers).

References

[1] CHARLES W. RUDY, Mid-IR Lasers: Power and pulse capability ramp up for mid-IR lasers, LaseFocusWorld (2014-05-02).

[2] Rebecca B. Andersen, Joshua Miller, Astonishingly Short Mid-infrared Pulses Offer New Tool for Peering Inside Atoms and Solids, Optical Society (2016-09).

[3] B. E. A. Saleh, M. C. TEICH, FUNDAMENTALS OF PHOTONICS (second edition), Wiley Series in Pure and Applied Optics, P886 (2007).

[4] Andrius Baltus'ka, Takao Fuji, and Takayoshi Kobayashi, Controlling the Carrier-Envelope Phase of Ultrashort Light Pulses with Optical Parametric Amplifiers, PhysRevLett.88.133901 (2002-03-18).

[5] Hauri, C., Kornelis, W., Helbing, F. et al, Generation of intense, carrier-envelope phase-locked few-cycle laser pulses through filamentation, Phys B 79: 673. doi:10.1007/s00340-004-1650-z (2004). B 79(6), 673–677 (2004).

[6] T. Morioka, K. Mori, and M. Saruwatari, More than 100-wavelength-channel picosecond optical pulse generation from single laser source using supercontinuum in optical fibres, Elect. Lett. 29, 862–864 (1993).

[7] R. R. Alfano and S. L. Shapiro, Observation of self-phase modulation and small-scale filaments in crystals and glasses, Phys. Rev. Lett. 24, 592–594 (1970).

[8] H. Delbarre and M. Tassou, Atmospheric gas trace detection with ultrashort pulses or white light continuum, in Conference on Lasers and Electro-Optics Europe, p. CWF104 (2000).

[9] David J. Jones, Scott A. Diddams, Jinendra K. Ranka, Andrew Stentz, Robert S. Windeler, John L. Hall, Steven T. Cundiff, Carrier-Envelope Phase Control of Femtosecond Mode-Locked Lasers and Direct Optical Frequency Synthesis, Physics Faculty Contributions (2000-04-28).

[10] A. Couairona, A. Mysyrowiczb, Femtosecond filamentation in transparent media, Physics Reports 441(2007)47–189 (2007-03).

[11] A. Couairona, A. Mysyrowiczb, Femtosecond filamentation in transparent media, PhysicsReports, Vol 441, Isss 2–4, Pgs 47-190, (2007-03)

[12] B. E. A. Saleh, M. C. TEICH, FUNDAMENTALS OF PHOTONICS (second edition), Wiley Series in Pure and Applied Optics, P895 (2007).

[13] B. E. A. Saleh, M. C. TEICH, FUNDAMENTALS OF PHOTONICS (second edition), Wiley Series in Pure and Applied Optics, P861 (2007).

[14] D. Milam, M. J. Weber, and A. J. Glass, Nonlinear refractive index of fluoride crystals, Appl. Phys. Lett. 31, 822-824 (1977).

[15] D. Milam, M.J. Weber, A.J. Glass, Appl. Phys. Lett. 31, 822 (1977)

[16] G. Duchateau, G. Geoffroy, A. Dyan, H. Piombini, and S. Guizard, Phys. Rev. B 83, 075114 (2011).

[17] T. Schnrider, Nonlinear Optics in Telecommunications, ISSN 1439-2474, P333 (2004).

[18] S. P. Singh, N. Singh, NONLINEAR EFFECTS IN OPTICAL FIBERS: ORIGIN, MANAGEMENT AND APPLICATIONS, Progress In Electromagnetics Research, PIER 73, 249–275 (2007)

[19] A. Major, F. Yoshino, I. Nikolakakos, J.S. Aitchison, P.W.E. Smith, Opt. Lett. 29, 602 (2004)

[20] W. Koechner, Solid-State Laser Engineering (Springer, Berlin, 2006)

[21] A.G. Selivanov, I.A. Denisov, N.V. Kuleshov, K.V. Yumashev, Appl. Phys. B 83, 61 (2006)

[22] Almaz Optics, Inc, MAGNESIUM FLUORIDE.

[23] Emiliano Cadelano and Giancarlo Cappellini, Electronic structure of fluorides: general trends for ground and excited state properties, European Physical Journal B Volume: 81 Issue: 1 Pages: 115-120 (2011-05).

[24] N. K. M. Naga Srinivas, S. Sree Harsha, and D. Narayana Rao, Femtosecond supercontinuum generation in a quadratic nonlinear medium (KDP), Vol. 13, Issue 9, pp. 3224-3229 (2005).

[25] ALKOR crystal optics, BARIUM FLUORIDE: BaF_2 windows and BaF_2 lenses.

[26] Alexander Q. Wu, Ihtesham H. Chowdhury, and Xianfan Xu, Femtosecond laser absorption in fused silica: Numerical and experimental investigation, PhysRevB.72.085128 (2005-08-22).

[27] M. Bradler, P. Baum, E. Riedle, Femtosecond continuum generation in bulk laser host materials with sub-μJ pump pulses, Appl Phys B (2009) 97: 561–574 (2009-08-21).

[28] B. E. A. Saleh, M. C. TEICH, FUNDAMENTALS OF PHOTONICS (second edition), Wiley Series in Pure and Applied Optics, P896 (2007).

[29] Marburger, J. H, Self-focusing: Theory, Progress in Quantum Electronics, Volume 4, Part 1, Pages 1-110 (April 1975).

[30] E. L. DAWES, J. H. MARBURGER ,Computer Studies in Self-Focusing, Phys. Rev. 179, 862 (1969-03-15).

[31] Kazimierz Rzazewski and Rainer Grobe, Saturation of Continuum-Continuum Transitions in Multiphoton Absorption, Phys. Rev. Lett. 54, 1729 (1985-04-15).

[32] A. Couairona, A. Mysyrowiczb, Femtosecond filamentation in transparent media, PhysicsReports 441(2007)47–189, P8 (2006-12-15).

[33] J. A. Fleck, Jr., J. R. Morris, and M. D. Feit, Time-Dependent Propagation of High EnergyLaser Beams through the Atmosphere, Appl.Phys. 10,129-160 (1976-02-09).

[34] A. Couairona, A. Mysyrowiczb, Femtosecond filamentation in transparent media, PhysicsReports 441(2007)47–189, P56 (2006-12-15).

[35] Yu. P. Raizer, BREAKDOWN AND HEATING OF GASES UNDER THE INFLUENCE OF A LASER BEAM, Sov. Phys. Usp. 8 650–673 (1966).

[36] R. H. Stolen, J. P. Gordon, W. J. Tomlinson, H. A. Haus, Raman response function of silica-core fibers, Journal of the Optical Society of America B Vol. 6, Issue 6, pp. 1159-1166 (1989).

[37] A. Couairona, A. Mysyrowiczb, Femtosecond filamentation in transparent media, PhysicsReports 441(2007)47–189, P74-75 (2006-12-15).

[38] Stefan Skupin, Gero Stibenz, Luc Bergé, Falk Lederer, Thomas Sokollik, Matthias Schnürer, Nickolai Zhavoronkov, and Günter Steinmeyer, Self-compression by femtosecond pulse filamentation: Experiments versus numerical simulations, Phys. Rev. E 74, 056604 (2006-11-06).

[39] B. E. A. Saleh, M. C. TEICH, FUNDAMENTALS OF PHOTONICS (second edition), Wiley Series in Pure and Applied Optics, Nonlinear Optics, Coupled-Wave Equation, P906 (2007).

[40] Robert W. Boyd, Nonlinear Optics (Third Edition), Wave-Equation Description of Nonlinear Optical Interactions, P72, Academic express, ISBN: 978-0-12-369470-6 (2008).

[41] Joshua E. Rothenberg, Space–time focusing: breakdown of the slowly varying envelope approximation in the self-focusing of femtosecond pulses, Opt. Lett. 17(8) 583-585 (1992).

[42] B. E. A. Saleh, M. C. TEICH, FUNDAMENTALS OF PHOTONICS (second edition), Wiley Series in Pure and Applied Optics, P88 (2007).

[43] RP Photonics Encyclopedia, Laser-induced Damage

[44] Roger M. Wood, Laser-induced Damage of Optical Materials, Inst. of Physics Publishing (2003).

[45] Crystran Ltd - World Wide Optics Source, Magnesium Fluoride.

[46] Crystran Ltd - World Wide Optics Source, Calcium Fluoride.

[47] Crystran Ltd - World Wide Optics Source, Barium Fluoride.

[48] Crystran Ltd - World Wide Optics Source, Yttrium Aluminium Garnet.

[49] Accuratus Corporation, Fused Silica, Glass Properties.

[50] Janis Research, Sapphire.

[51] Eksmaoptics, Potassium dideuterium PhosPhate.

[52] Miguel Miranda, Cord L. Arnold, Thomas Fordell, Francisco Silva, Benjamin Alonso3 Rosa Weigand4 Anne L'Huillier, and Helder Crespo, Characterization of broadband few-cycle laser pulses with the d-scan technique, Opical Express, Vol. 20, Issue 17, pp. 18732-18743 (2012).

[53] V. V. Lozovoy, I. Pastirk, and M. Dantus, Multiphoton intrapulse interference. IV. Ultrashort laser pulse spectral phase characterization and compensation, Opt. Lett. 29(7), 775–777 (2004).

[54] J. A. Nelder, The Analysis of Randomized Experiments with Orthogonal Block Structure. II. Treatment Structure and the General Analysis of Variance, The Royal Society, 283(1393):147-162 (1965-01-06).

[55] Anne-Laure Calendron et al, White-light generation with sub-ps pulses, Opt. Express, Vol. 23, Issue 11, pp. 13866-13879 (2015).

[56] D. Paipulas, A. Balskiene, and V. Sirutkaiti ,EXPERIMENTAL STUDY OF FILAMENTATION AND SUPERCONTINUUM GENERATION IN LASER-MODIFIED FUSED SILICA, Lithuanian Journal of Physics, Vol. 52, No. 4, pp. 327–333 (2012).

[57] Haiyi Suna, Tianqing Jiaa, Chengbin Lia, Xiaoxi Lia, Shizhen Xua, Donghai Fenga, Xiaofeng Wanga, Xiaochun Gea, Zhizhan Xua, Mechanisms of femtosecond laser-induced damage in magnesium fluoride, Solid State Communications, 141 (2007) 127–131 (2006-10-13).

[58] Valdas Sirutkaitis, Laser-Indeuced-Damage in Ultra fast Laser Systems, Valdas Sirutkaitis, (2013-06-23).

[59] Philippe Rigaud, Aymeric Van de Walle, Marc Hanna, Nicolas Forget, Florent Guichard, Yoann Zaouter, Khmaies Guesmi, Frédéric Druon, and Patrick Georges, Supercontinuum-seeded few-cycle mid-infrared OPCPA system, Opt. Express, 24(23):273228 (2016).